2014

Pressure and Temperature Response of a Stimuli-Responsive Polymer Probed with Raman Microscopy

Coleman Cariker
University of Central Florida

Recommended Citation

Cariker, Coleman, "Pressure and Temperature Response of a Stimuli-Responsive Polymer Probed with Raman Microscopy" (2014). *HIM 1990-2015*. 1661.
https://stars.library.ucf.edu/honorstheses1990-2015/1661

PRESSURE AND TEMPERATURE RESPONSE OF A STIMULI-RESPONSIVE POLYMER PROBED WITH RAMAN MICROSCOPY

by

COLEMAN CARIKER

Spring 2014

Abstract

Poly(N-isopropylacrylamide) (PNIPAM) is a thermo-responsive hydrogel; that is, it is a macromolecule which exists in a hydrated state beneath its lower critical solution temperature (LCST). Polymers such as PNIPAM undergo a phase transition in response to changes in temperature, pressure, pH, salt concentration, and the addition of co-solvents. Previously, visible-light microscopic measurements of the pressure-induced phase transition have been hindered by the lack of a pressurization apparatus with the short working distance and optical transmission properties necessary for high resolution microscopy. We employ a high pressure setup which uses a fused silica micro-capillary to contain the sample. Our experiment reveals differences in the spatial evolution of the phase change across the temperature and pressure thresholds, and Raman measurements allude to conformational differences in the evolution of the phase transitions. The Raman peaks positions are in agreement with previous FTIR measurements, and due to a difference in selection rules additional vibrational bands are observed in the Raman spectra.

Acknowledgements

A special thanks to my mentor, Dr. Schulte, for his guidance, support, and endless patience in guiding me through the thesis writing process. Furthermore, a thanks to the Chair for functional materials, TU Munich, for providing the polymer samples. Also, my gratitude goes out to my thesis committee and Dr. Lunsford for providing invaluable feedback during the writing process.

I would also like to express my eternal love and gratitude for my family: my wife, Emilye, for providing the encouragement, support, and faith in my abilities needed to press on, and my daughter, Kennedy, the inspiration for everything that I do. Without you two none of this would be possible.

Table of Contents

List of Tables

List of Figures

1.Introduction

PNIPAM is a thermo-responsive polymer that is characterized by a sharp phase transition that occurs at approximately 32^oC, notably in the vicinity of the normal human body temperature. During this process the molecule undergoes a dramatic transition, expelling its hydration water and changing configuration from random coil to globular. (1) While most often a phase change is induced by temperature fluctuation, it is also possible induce a phase separation by applying pressure. Because of these properties, PNIPAM has become a model system for studying multifunctional smart materials that undergo similar volume phase transitions. (2) (3) These materials have been developed for medical uses such as controlled drug release, artificial muscles, and skin grafting. (4) (5) The versatility of these materials stems from the ability to tune the phase transition with stimuli such as temperature differences, electric fields, solvent concentration, or the addition of salts. (3) Furthermore, proteins have similar properties to hydrogels, unfolding from their native globular configuration below a certain temperature. This behavior, cold denaturation, is nearly the reverse of the PNIPAM hydrogels, which are hydrated in their relaxed state. Previous FTIR results show that spectroscopic shifts in the amide I' bands of PNIPAM are also observed in proteins undergoing similar phase transitions. (6) Also, molecules such as PNIPAM have spectra that can be interpreted more readily than the spectra arising from the complex structure of proteins. In particular, analysis of the amide group in PNIPAM is simplified since the polymer is composed of a C-H backbone, with the amide groups situated on the side chains. (1) In contrast, the amide groups constitute the backbone of proteins, causing the amide spectra to be sensitive to the secondary structure of the molecule. Lastly, the cold denaturation process in proteins typically occurs below the freezing point of water, complicating observation. (7) Studies of the phase transition of PNIPAM may therefore contribute to models of the cold denaturation of proteins. (6) (8) (9)

In this thesis we begin by providing a background in the theory describing the phase separation of polymers in solution. We then give a description of spectroscopic methods, elaborating on our particular experimental setup. Next, we present our Raman and optical microscopic measurements of PNIPAM across the temperature and pressure-induced phase transition, focusing on the spectral regions which show changes across the transition. Finally, we will analyze our results, comparing with FTIR data from similar experiments.

1.1 Polymer Entropy of Mixing

The entropy S of a substance is defined by the number of configurations the particles in a system can assume, specifically

$$S = k_B \ln \Omega$$

Where Ω is the multiplicity of the system. A polymer is a molecule built from a succession of identical segments, joined together by a backbone of C-C bonds. This allows the polymer to adopt a large range of conformations, owing to the numerous rotations that can occur at these bonds. In a solution, the polymer molecules adopt the state of lowest energy, a highly degenerate random coil configuration. When considering the entropy of a polymer, a 2 dimensional lattice can be used to represent the spatial configuration of particles, drawn with one monomer segment at each site and lines representing the covalent bonds of the molecular backbone linking the segments together. Ω is then the number of possible configurations the polymer can assume on the lattice. (10)

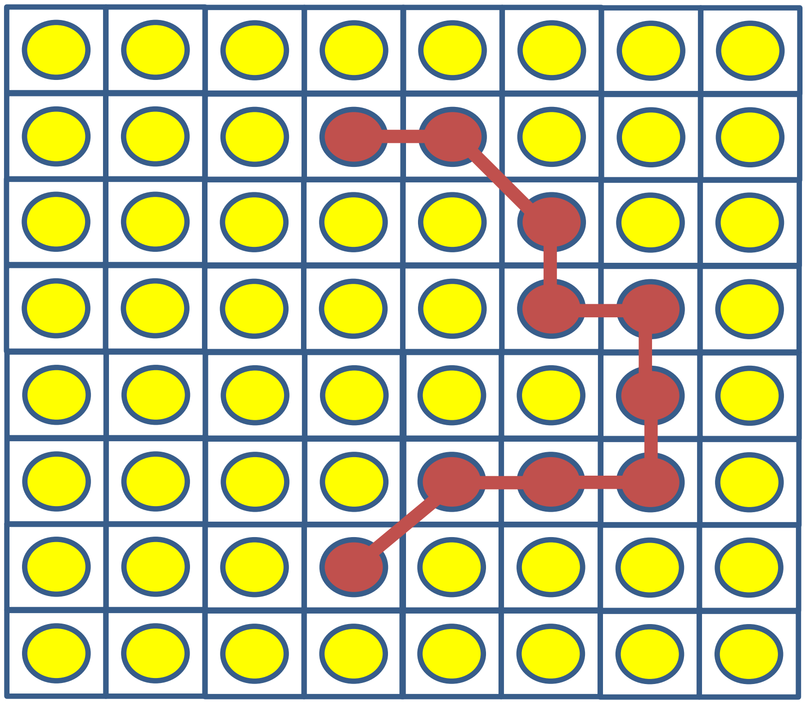

Figure 1: Two-dimensional lattice model of polymer molecule in solution, showing one possible configuration

When using this method to calculate the entropy there are 3 assumptions made: 1) that there are no interactions between particles, 2) only one particle can occupy a lattice site, and 3) that all of the lattice positions must be occupied. Then, following the derivation by Flory (11):

$$\Omega = \frac{1}{n_2!}\prod_{i=1}^{n_2} \nu_i$$

where ν_i is the number of possible configurations of the i^{th} polymer chain and n_2 is the number of polymer chains belonging to the system, one can arrive at

$$S = \ -k_B[n_1 \ln \frac{n_1}{n_1 + Nn_2} + n_2 \ln \frac{n_2}{n_2 + Nn_1} - n_2(N-1)\ln \frac{z-1}{e}$$

where N is the number of monomers per polymer chain, z is the coordination number, and n_1 is the number of solvent molecules. The total entropy of the system is the sum of the entropy of mixing and the conformational entropy which arises from differences between the polymer molecules, however if we ignore the disordering entropy and consider one mole of an ideal polymer solution ($n_1 = 0$), then the entropy of mixing is

$$S_m = -R[\phi_1 \ln \phi_1 + \frac{\phi_2}{N} \ln \phi_2]$$

where ϕ_1 and ϕ_2 are the volume fractions of the two types of particles in the lattice. The enthalpy change is dependent on the properties of both the solvent and the solute, and is given by

$$\Delta H_m = k_B T N_1 \phi_2 \chi_{12}$$

where χ_{12} is a parameter introduced to describe the interactions between solvent and solute molecules. The Gibbs free energy change, which determines whether or not mixing will be spontaneous under certain conditions, is defined as

$$\Delta G_m = \Delta H_m - T\Delta S_m.$$

Assembling the previous expressions we arrive at the expression for the Gibbs free energy change for mixing a polymer with a solvent, we have

$$\Delta G_m = RT[n_1 \ln \phi_1 + n_2 \ln \phi_2 + n_1 \phi_2 \chi_{12}].$$

1.2 Model of Phase Separation of a Polymer in Aqueous Solution

Considering a polymer solution with Gibbs free energy change $\Delta \mathrm{G}(\phi)$, and the same solution separated into its two constituents with volume fraction α and β so that $\phi = \alpha\phi_\alpha + \beta\phi_\beta$, if an adiabatic system is in equilibrium then $\Delta \mathrm{G}(\phi)$ is minimal and thus phase separation will not occur as long as

$$\Delta \mathrm{G}(\phi) < \alpha \Delta G(\phi_\alpha) + \beta \Delta \mathrm{G}(\phi_\beta).$$

Figure 2 shows a graph of the Gibbs free energy as a function of the polymer concentrations at different temperatures. $\mathrm{B}_1 \text{and } \mathrm{B}_2$ denote the positions where $\frac{\delta \mathrm{G}}{\delta \phi}$ = 0. These positions define the binodal line, shown in blue on the lower graph. This line on the phase diagram denotes the point beyond which the single and two-phase states exist in equilibrium. $\mathrm{S}_1 \text{and } \mathrm{S}_2$ show the inflection points where $\frac{\delta^2 \mathrm{G}}{\delta \phi^2}$ = 0. These points give the locations of local stability, where $\frac{\delta^2 \mathrm{G}}{\delta \phi^2} > 0$, defining the spinodal line (shown in red) on the phase diagram. Between the binodal and spinodal lines the solution is metastable and demixing typically requires the presence of impurities; that is, nucleation and growth *may* occur. Note that the system has a lower critical solution temperature, or LCST, at $\mathrm{T} = \mathrm{T}_\mathrm{c}$, where the regions of stability disappear and the solution is forced to phase separate.

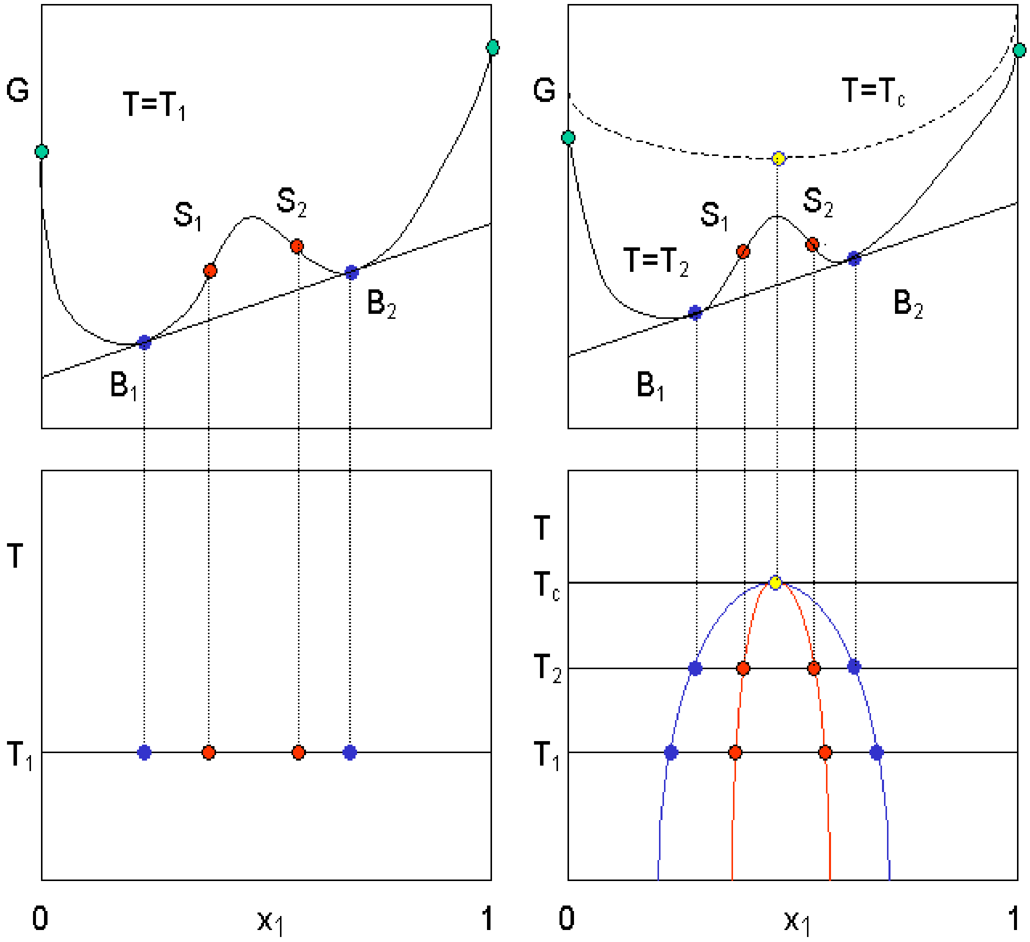

Figure 2: Gibbs free energy as a function of concentration (upper) and T vs. concentration diagram showing stable and unstable regions (lower) (12)

Beneath the spinodal line, a homogeneous solution is unstable against microscopic fluctuations in density or composition and there is no thermodynamic barrier to the growth of a new phase; that is, the phase transition is modulated solely by diffusion. Due to this simplification, the process can be modeled by an approximate analytical solution to the general diffusion equation. (13) Numerical simulations modeling the evolution of spinodal decomposition are shown in Figure 3. Our interest in these models will soon become apparent.

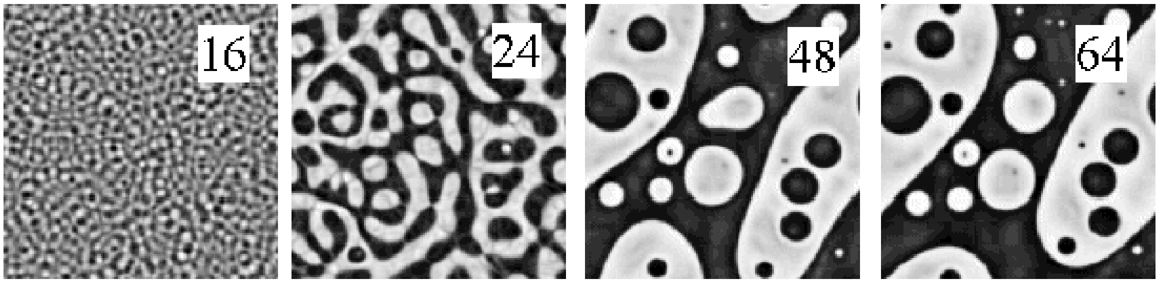

Figure 3: Numerical simulation of spinodal decomposition, evolving left to right (14)

1.3 The Phase Transition of PNIPAM

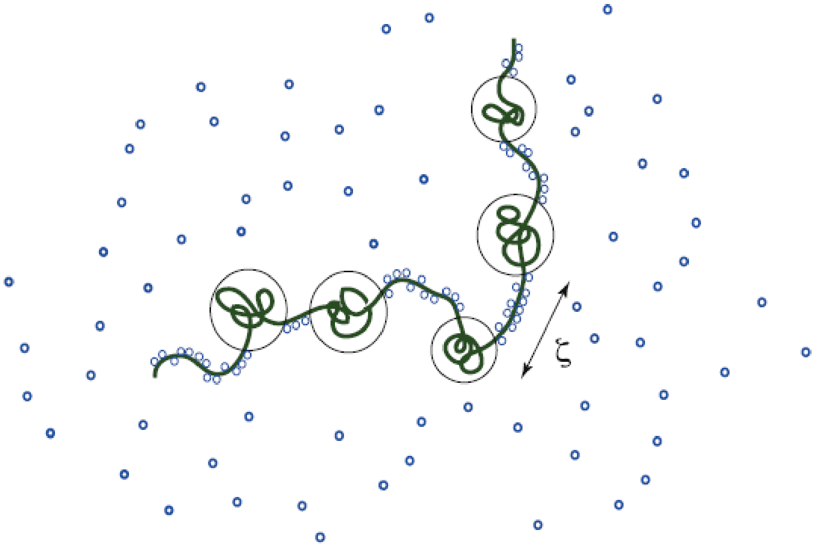

Figure 4: Model of PNIPAM polymer, showing monomer-monomer, polymer-solvent, and solvent-solvent interactions. (15)

Although simple when compared to biomolecules like proteins, current theoretical models fail to comprehensively predict the LCST behavior of PNIPAM. (1) This failure results from the complicated interactions taking place between the hydrophilic C=O and N-H, hydrophobic methyl groups, and the bound water (see Figure 4), all of which contribute to the χ_{12} parameter contained in the entropy of mixing and enthalpy.

Two species of bound water have been suggested to exist within a PNIPAM solution, one type bound to the hydrophilic amide group, and the other belonging to the water surrounding the hydrophobic moiety found on the side group. (16) (17) The latter forms a clathrate structure around the methyl molecules, reducing the coordination of the water molecules (the number of hydrogen bonds per molecule), and thus increasing the order of the water molecules. This decrease in entropy is balanced by the decreased order associated with the highly degenerate random coil structure of the polymer, as opposed to being in a more ordered, folded state. The water molecules bound to the amide group through hydrogen bonding provide a nucleation site for more water molecules, thought to have a cooperative stabilizing effect on the hydration of the polar groups. (3) The phase separation is thought to occur when the unfavorable entropy associated with the orderly arrangement of water molecules around the hydrophobic groups overcomes the stabilization provided to the solvated polymer by the water molecules bound to the amide group. (18) (19) Studies have shown that the number of water molecules bound to the N-H and C=O sites decreases from roughly 11 below the LCST to 2 above, resulting in the adoption of a compact structure which minimizes the hydrophobic groups’ interface with the solvent. (20) While the mechanism for the pressure induced phase transition has also been investigated (3) (6) (21), spectroscopic analysis has previously been limited to infrared absorption experiments. In particular, high resolution microscopic measurements of PNIPAM under pressure have not been previously performed due to the lack of a pressurization apparatus with the requisite optical transmission properties. Intense interest remains in elucidating the exact nature of the interactions of PNIPAM with solvent, both to further materials technologies as well as to provide a more fundamental understanding of the complex interactions governing the function of biomolecules and the behavior of polymers in solution. (9) (21) (17)

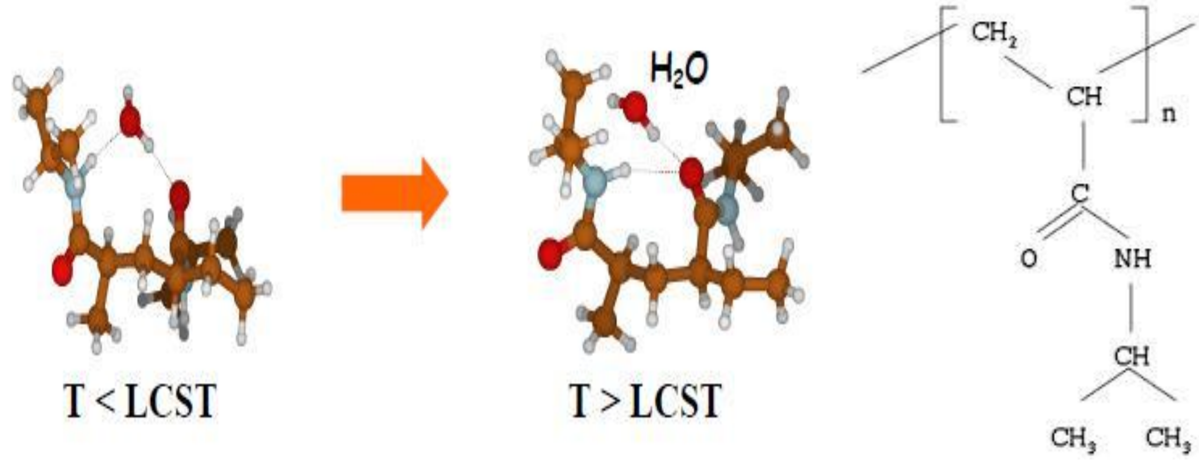

Figure 5: molecular depiction of phase transition (left) (2), skeletal structure of PNIPAM molecule segment (right) (1)

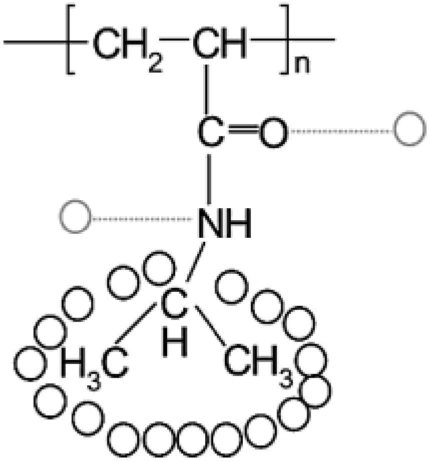

Figure 6: Depiction of the two types of bound water hypothesized in PNIPAM. Water bound to the hydrophilic amide group stabilizes the solvation of the molecule, while the ordered water molecules around the methyl groups adds an entropic penalty to solvation. (17)

1.4 Raman Spectroscopy

First demonstrated in 1928 By Krishna and Raman (22), Raman spectroscopy has since been refined and is now a widely employed method due to the sensitivity to changes in molecular structure (amongst other things). The theory of Raman scattering is complimentary to the somewhat simpler but more well-known theory of infrared (IR) absorption. IR absorption occurs when the energy of the incident photon is such that there is a resonance effect with the vibrational modes of the molecule. When this occurs the incident photon is absorbed, its energy converted into vibrational energy in the molecule. By contrast, Raman scattering is a two-photon event, occurring when the excitation from the incident radiation modulates the polarizability tensor of the molecule, causing an induced dipole moment in the molecule. The strength of the polarization is proportional to the polarizability α and the electric field E:

$$P = \alpha E.$$

Considering an excitation source with a field given by

$$E = E_0 \cos 2\pi \nu_0 t$$

where $\nu_0$is the frequency of the laser. Then the molecular vibrational normal modes $Q_j$are given by

$$Q_j = Q_j^{\circ} \cos 2\pi \nu_j t$$

where ν_j is the characteristic harmonic frequency of the jth normal mode. For a molecule with N atoms, there are 3N-6 (or 3N – 5 for a linear molecule) normal modes. The radiation emitted by this induced dipole contains both elastically (Rayleigh) scattered radiation and inelastically (Raman) scattered light. The Raman scattered light differs in energy from the Rayleigh scattered light by the vibrational energy that is gained or lost by the molecule. The polarizability of the molecule is modulated by the molecular vibration so that

$$\alpha = \alpha_0 + \left(\frac{\delta\alpha}{\delta Q_j}\right) Q_j + \cdots$$

Now when considering the previous, and noting that

$$\cos a \cos b = \frac{[cos(a+b) + \ cos(a-b)]}{2},$$

neglecting higher order terms we have:

$$P = \alpha_0 E_0 \cos 2\pi\nu_0 t + E_0 Q_j \left(\frac{\delta\alpha}{\delta Q_j}\right)\left(\cos 2\pi\left(\nu_0 + \nu_j\right)t + \cos 2\pi\left(\nu_0 - \nu_j\right)t\right)/2.$$

Note that as a consequence of the above, there will be both positive and negative Raman shifts. Also, this equation suggests that polarization and scattering are linear with the laser intensity (non-linear scattering can occur with high values of E_0 but is not normally a concern in analytical applications). Also, only vibrations that change the polarizability will yield Raman scattering. Lastly, $\left(\frac{\delta\alpha}{\delta Q_j}\right)$ is generally much smaller than α_0, so that Raman scattering is much weaker than Rayleigh scattering. If the energy of the excitation source is close to an electronic transition energy of the molecule, then resonance Raman scattering is observed. This results in a resonance enhanced signal that is orders of magnitude more intense than ordinary Raman scattered light. (23)

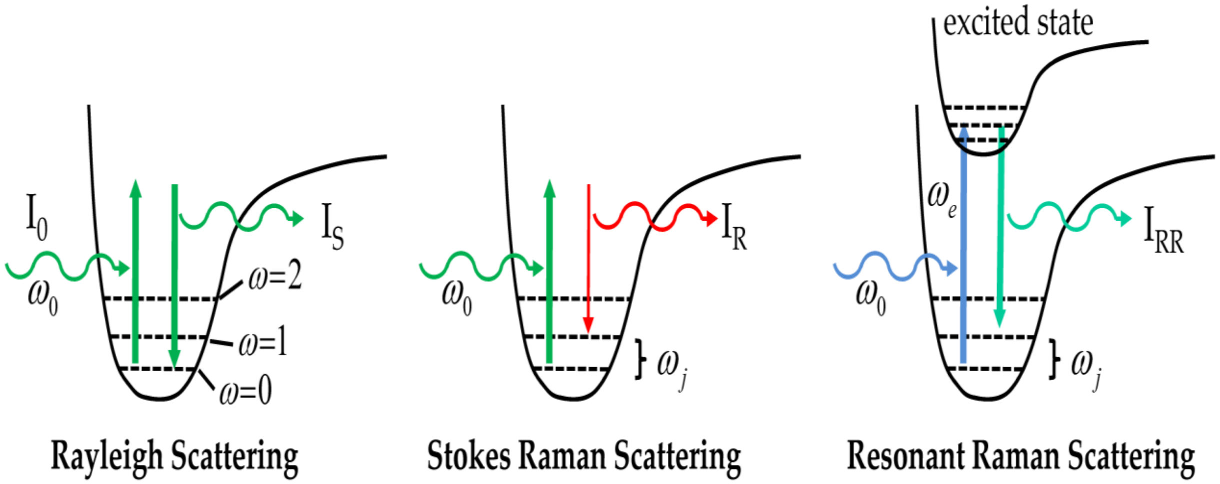

Figure 7: Diagram of vibrational energy levels showing different types of scattering. (24) (25)

1.5 Raman Microscopy

Raman microscopy is the application of Raman spectroscopy to small samples, or to localized volumes in a larger sample, and is inherently more technically challenging than traditional Raman scattering measurements for several reasons. One reason is that microscopic samples with a large surface area-to-volume ratio typically have a much more intense Rayleigh signal relative to the Raman scattering intensity than their macroscopic counterparts. For example, consider a polyethylene sphere 1 micrometer in radius. The Raman scattering intensity for this sphere is estimated to be 10^{12} times smaller than the Rayleigh scattered intensity. This is roughly the equivalent of trying to see the light from a firefly at a distance of 1m, if said firefly was superimposed onto the midday sun. (26) Therefore, Raman applications were limited prior to the development of monochromatic, directed light (laser) excitation sources. Even then, Raman microscopy was not commonly used until the advent of the highly efficient notch filters, CCD detectors, and simplifications to spectrometers. The improvements to Raman microscopy made by recent technological advances cannot be understated-most modern

Raman setups sold currently come equipped with a microscope. A Raman microscopy setup uses a microscope to focus the laser beam, and includes a pinhole or slit to provide confocal resolution as well as resolution in the XY plane. This enhanced resolution makes Raman microscopy especially suited to studying particular regions of larger biological assemblies such as cells, as well as acquiring spectra from a thin film atop a substrate. (27) The drawbacks of this type of experimental setup include limitations on sample size/geometry (it must fit into the microscope), and the short working distance required by the optics.

2. Experimental Procedures

2.1 Experimental Setup

Our experimental setup consists of a customized Raman microscopy system currently incorporating a 633nm HeNe excitation source, however a 785nm diode and 442nm HeCd laser are also included in the setup and can be interchanged with minimal effort. The novelty of the setup lies in the ability to perform Raman microscopy under pressure using a visible excitation source. This apparatus employs a hydraulic pressurization device connected via a series of low-volume tubing to an interchangeable micro-capillary, which contains the sample. (28) Ethanol was used as a pressurizing medium; the application of hydrostatic pressure permitted the sample pressure to be measured by a Bourdon pressure gauge connected to the system. The micro-capillary is made of fused silica, due to its strength and favorable optical transmission properties. With this apparatus it is possible to pressurize samples to > 400MPa, while maintaining the ability to perform optical and spectroscopic measurements through the wall of the capillary tube. The small volume of the capillary allows it to withstand a large pressure while still having a wall thickness small enough to accommodate the short working distance demanded by the Raman microscopy setup. This setup allows us to monitor PNIPAM and other macromolecules under pressure using visible microscopic measurements, probing the phase transition with methods previously inaccessible. It should also be noted that a temperature-controlled (with circulating water) copper slide was fabricated to house the micro-capillary, so that the temperature induced phase transition could be observed in the (otherwise) same conditions as the pressure induced case.

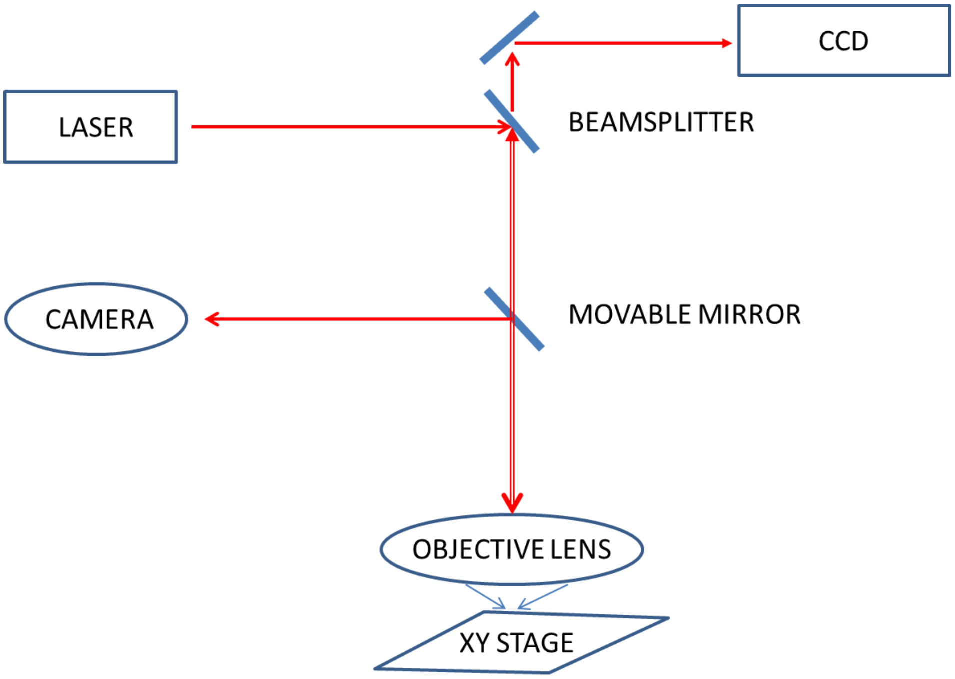

Figure 8: Raman microscopy setup in lab (pressurization apparatus not shown).

2.2 Procedure

PNIPAM samples were first obtained with the assistance of the Chair for Functional Materials, Physics department, TU Munich, and further PNIPAM polymer was purchased from Sigma Aldrich. The samples used in experiment were 25% wt. PNIPAM dissolved in D_2O. After dissolving, PNIPAM samples were agitated at 400 rpm overnight to ensure adequate mixing. After storage, samples were agitated at 400 rpm for an hour prior to examination. For both Raman and optical measurements, the sample was placed inside a fused silica capillary tube having a 75um inside diameter and a 96um wall thickness. Calibration of the spectrometer was performed using a Neon lamp in the fingerprint region and using the Argon lines from the ambient fluorescent lighting to calibrate for the C-H region. A re-calibration was performed at the beginning of each day, as well as any time the spectrometer was repositioned, with a record of each calibration maintained.

3. Experimental Results

3.1 Optical Imaging of the Phase Transition

First, optical imaging of the temperature phase transition was performed. After preparing the sample inside a capillary tube, the sample was thermally coupled to a copper temperature-controlling slide (initially at room temperature). Observation of the sample under 50x magnification was carried out while slowly increasing the temperature from $20^o C$ to $50^o C$, then decreasing the temperature back to $20^o C$. The temperature of the sample was approximated to first order to be that of the circulating water, and the rate of change was kept under $0.5^o C$/minute to maintain thermal equilibrium between the sample and the copper slide. Later, this approximation was verified by attaching a PT100 resistance thermometer to the copper slide and measuring the resistance of the PT100 to monitor the temperature of the slide. The temperature reading on the thermometer and the temperature measured using the PT100 was found to be in agreement to within $3^o C$. The data was later adjusted to agree with the temperature calculated from the measured resistance of the PT100.

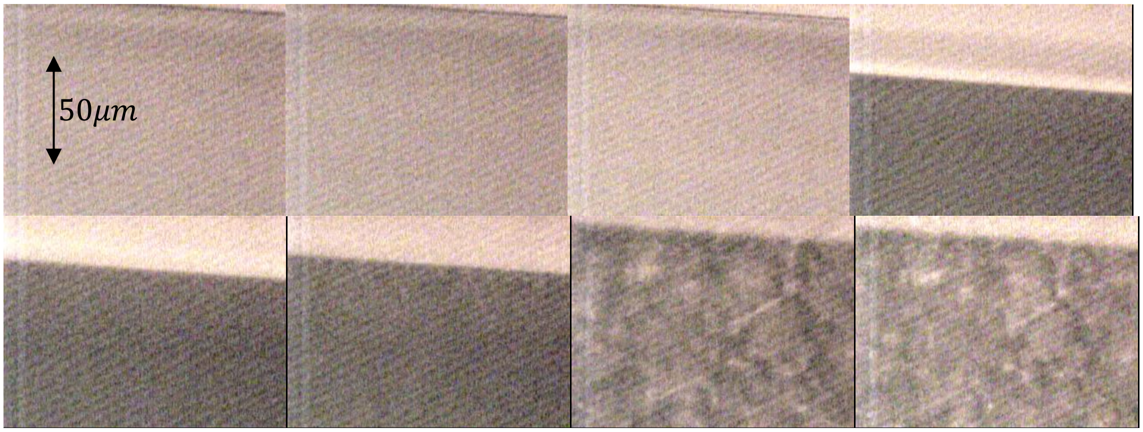

Figure 9: Optical imaging of PNIPAM at various temperatures: (right to left, top to bottom) 23, 27.5, 32, 33, 36, 38, 40, and $42^o C$.

The pressure induced phase transition was similarly observed. The sample was prepared inside a capillary tube which was then fitted into the hydrostatic pressurization apparatus. The sample was imaged as the pressure was increased to over 400MPa, with a phase transition observed around 240MPa.

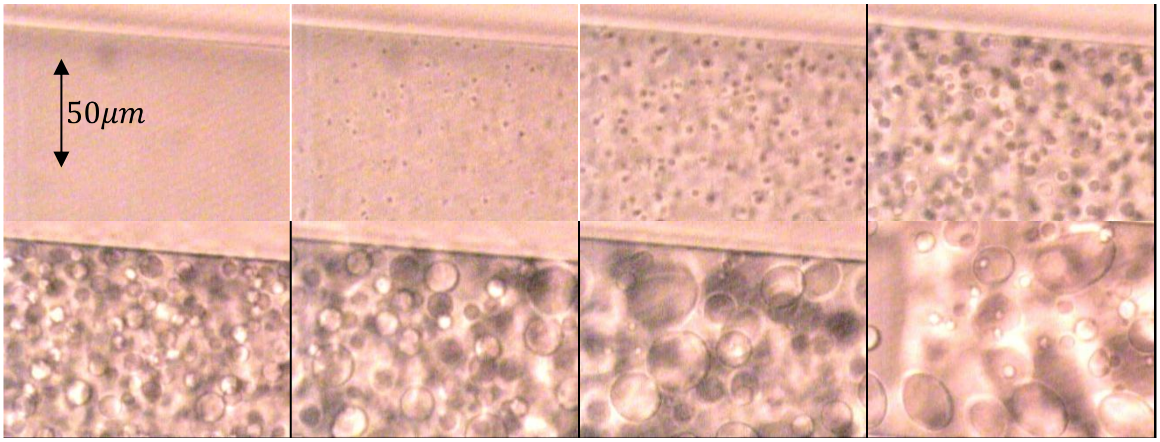

Figure 10: Optical imaging of PNIPAM across the pressure-induced phase transition, at pressures (right to left, top to bottom) 227.5, 244.8, 248.2, 255.1, 262.0, 268.9, 275.8, and 365.4MPa.

Optical observation of the pressure and temperature induced VPTs reveal differences between the two cases in the spatial evolution of the phase change. Worthy of note are the similarties between Figures 3 and 10; the pressure induced phase transition strongly resembles spinodal decomposition. To ensure the structures formed in Figure 10 were not due to sample contamination or some other artifact, the experiment was performed on multiple samples. The results were found to be reproducable. In contrast with pressure, the temperature induced phase transition appears spatially homogeneous. Microscopic imaging of PNIPAM at pressures up to 400MPa was reported by Kunugi et. al. (21), using the Teramecs high pressure cell, which incorporates 7mm thick sapphire windows through which to perform measurements. They do not report any phase separation at higher pressures, possibly because they used a 1% weight solution. They do, however, observe a re-hydration of the polymer chains at temperatures above the LCST with increased pressure. This suggests that higher pressures have a cooperative effect on the hydration of the polar groups, since it is known that the high pressure imposes an entropic penalty to the bound water surrounding the hydrophobic moieties. The P-T diagram for PNIPAM, determined through cloud point measurements by Otake et al., is shown below in Figure 11.

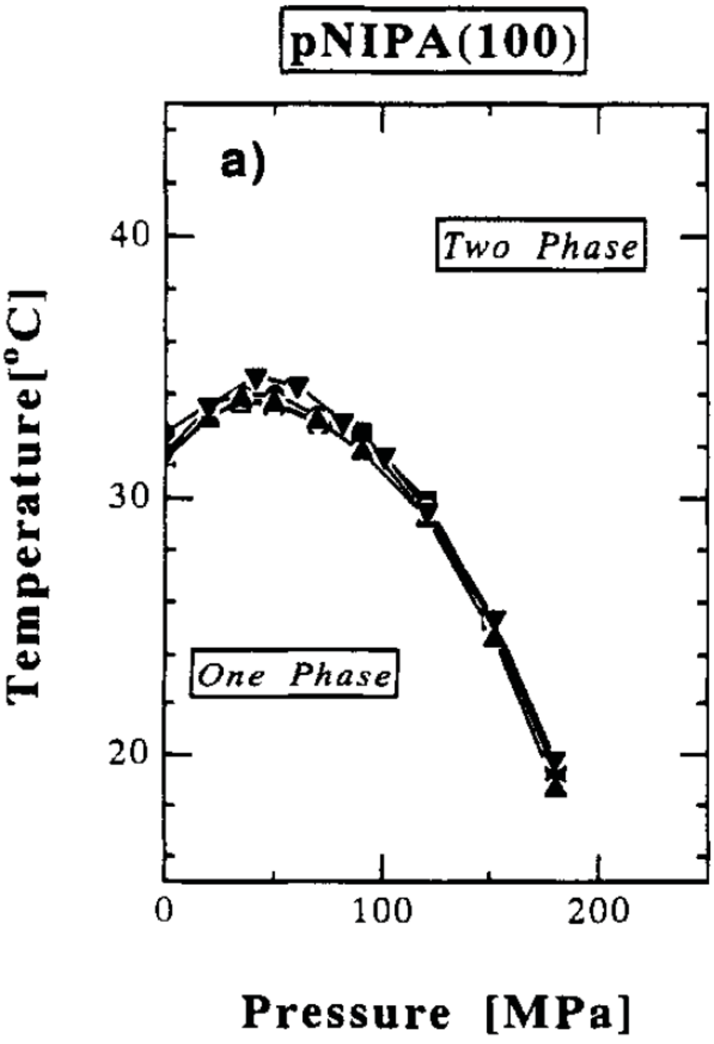

Figure 11: P-T of PNIPAM, determined using cloud point measurements. (28)

3.2 Spectroscopic Analysis of the VPT

Once visual observation of the sample had been performed, Raman microscopy measurements were then carried out on the sample. In order to determine spectral band assignments, a low resolution spectrum of the sample was obtained. Spectral bands were then compared with the various band assignments of the PNIPAM moieties found in other literature, compiled in Table 1.

Band Position (cm^{-1})	Assignment
2982	Asymmetric C-H stretching (a)
2940	Asymmetric C-H stretching of –CH_2 (b)
2920	Symmetric C-H stretching of – CH_2 (b)
2882	Symmetric C-H stretching (a)
1626	Amide I’ Region (C=O stretching)
1480	CH_3 asymmetric deformation (a)
1460	CH_2 asymmetric deformation (b)
1450	Assignment Pending
1391	CH_3 symmetric deformation (a)
1371	CH_3 symmetric deformation (a)
1133	CH_3 rocking (a)

Table 1: list of spectral band assignments, (a) denotes vibrations associated with the methyl group, (b) denotes modes associated with the molecular backbone. (6) (29)

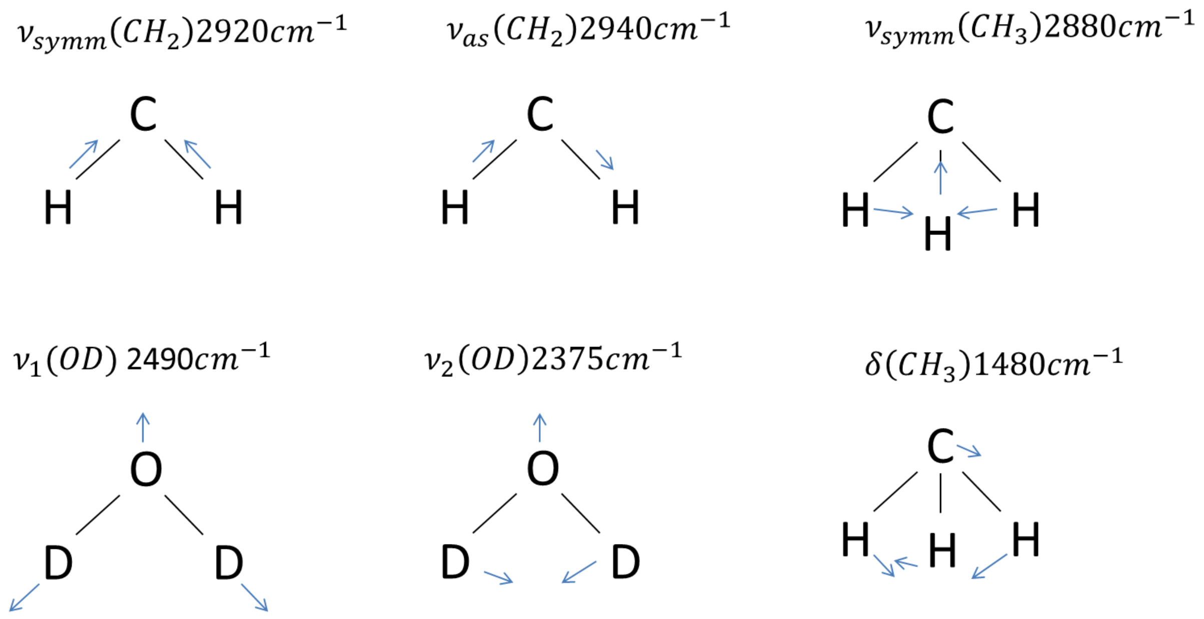

Figure 12: Diagram of some characteristic normal modes found in PNIPAM/$D_2O\ solution$. (25)

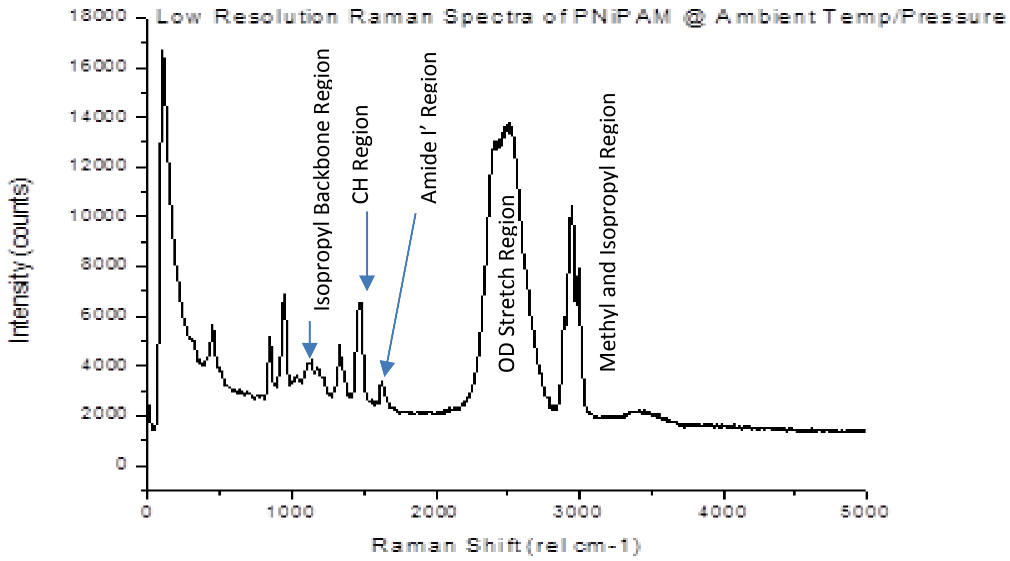

Figure 13: Low resolution spectra of PNIPAM temperature/pressure, without baseline correction.

Once an initial assignment of the various spectral bands from the PNIPAM sample under study was obtained, high resolution spectra were acquired across both the temperature and pressure induced phase transitions. Due to the increase in resolution, the range of observable spectra was diminished. Covering the entire spectral range required two separate acquisitions, observing the spectral changes in the fingerprint region in one acquisition then observing spectral contributions from the D_2O and the C-H regions in another. Figures 14 and 15 show a comparison between high resolution Raman and FTIR spectra of PNIPAM, demonstrating the complimentary nature of Raman and FTIR spectroscopy. Normal modes associated with Raman scattering are also tied to absorption frequencies, demonstrated by the many shared peak frequencies. The different selection rules for absorption and Raman scattering are noted by the different intensities and line shape observed for the same peak frequency, with some bands missing entirely from one or the other.

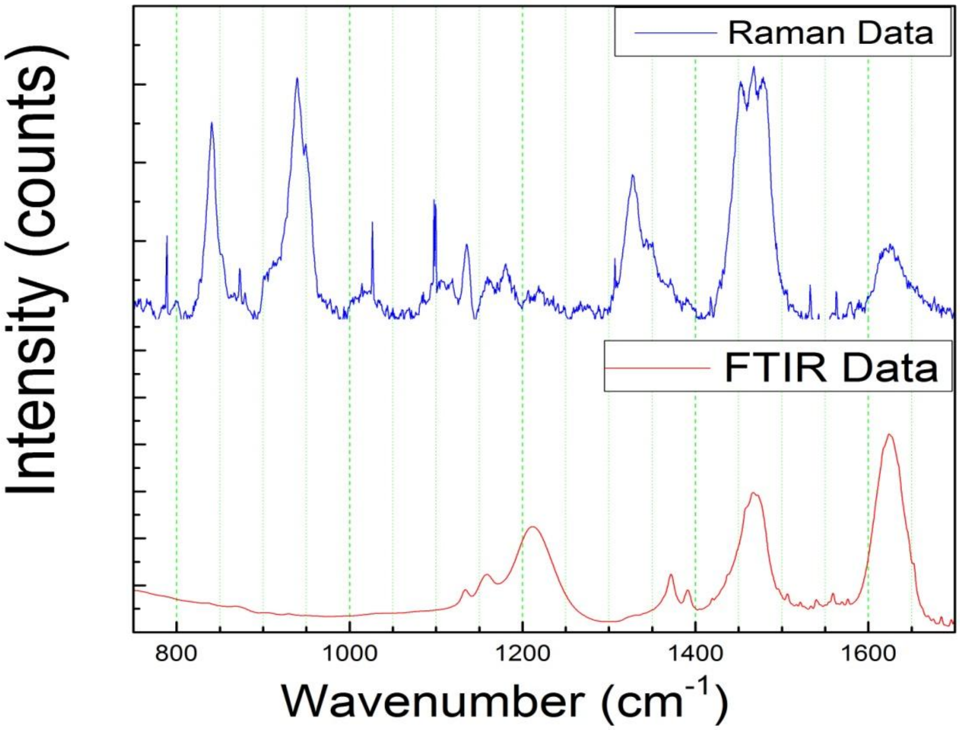

Figure 14: Comparison of Raman and FTIR spectra, showing the fingerprint region. (30)

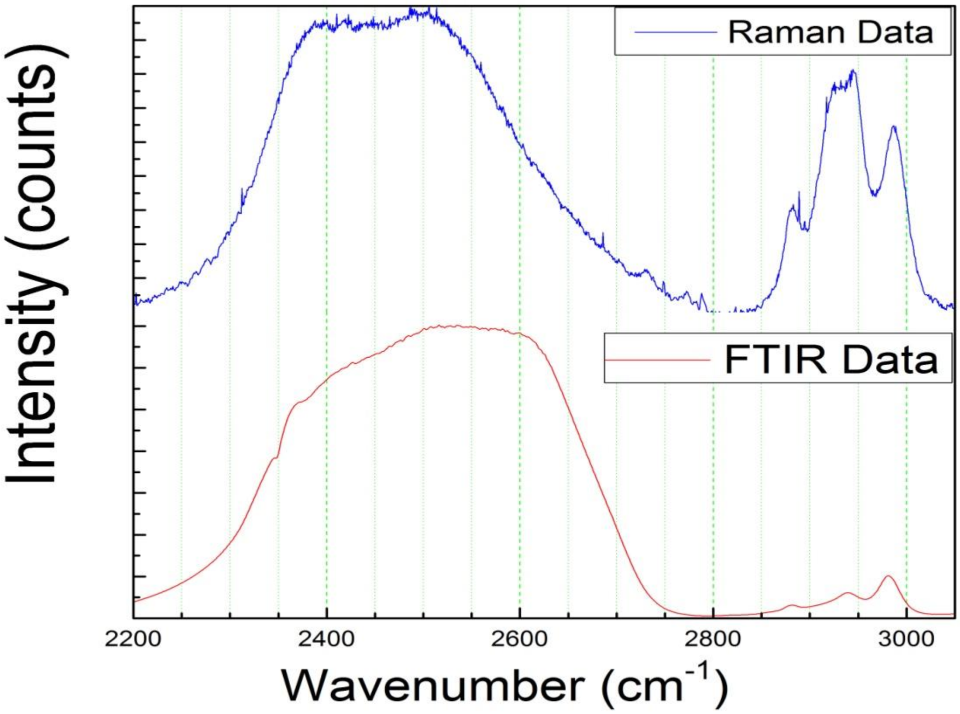

Figure 15: Comparison of Raman and FTIR spectra, showing the C-H region. (30)

3.2.1 Analysis of the Temperature Induced VPT

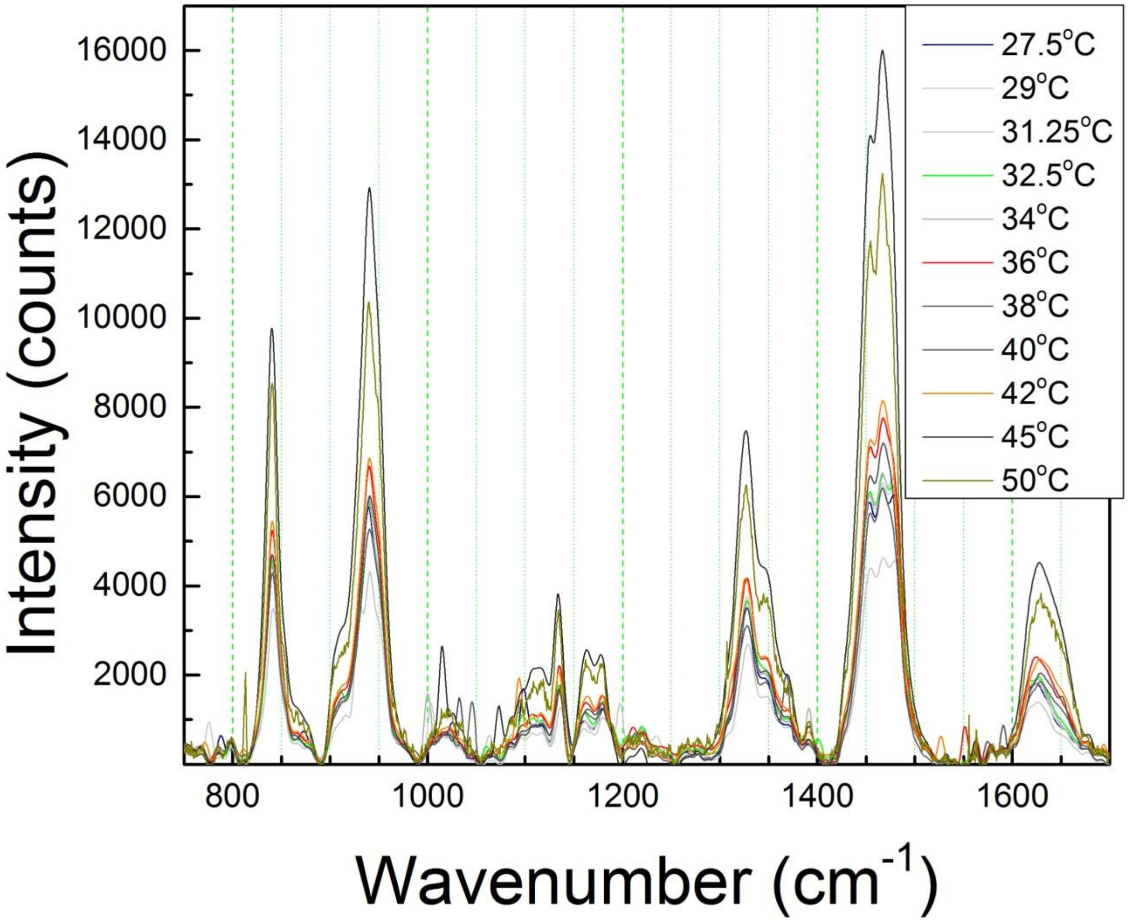

Figure 16: High-resolution Raman spectra in the spectral fingerprint region of PNIPAM inside a capillary at various temperatures, after baseline correction and FFT smoothing.

The high resolution Raman spectra of PNIPAM across the LCST transition contain some changes worth noting. Specifically, shifts in peak frequency and/or relative area can be seen in the fingerprint region around 1175, 1450, and $1625cm^{-1}$. The D_2O and C-H spectral regions at $\sim 2500cm^{-1}$ and $\sim 2900cm^{-1}$ also contain differences above and below the LCST, shown in Figure 13.

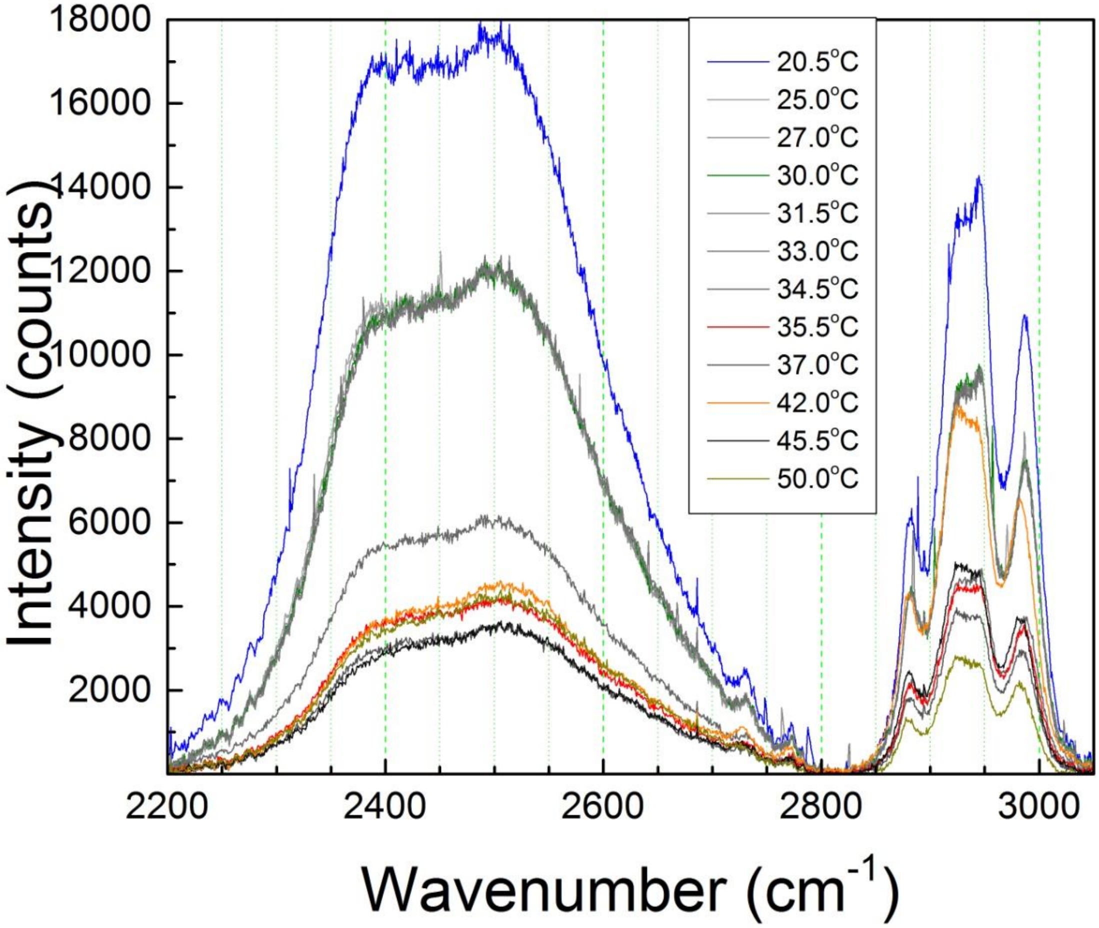

Figure 17: High resolution Raman spectra of PNIPAM at various temperatures, with grating centered at around 2620cm^{-1}, after baseline correction.

Once spectral regions of interest were identified, each group was isolated (Figure 18) and data analysis was performed using standard spectroscopic data analysis methods, outlined in the following. First, a baseline correction was performed on the data (Figure 19). This correction reduced the number of parameters in the subsequent fitting, resulting in more consistent results. Once a baseline correction had been performed, the data was smoothed using the Fast Fourier Transform method included in the analysis software (Figure 20). This smoothing also helped produce more consistent results in the analysis, and is justified by the similarity between the actual and the smoothed data.

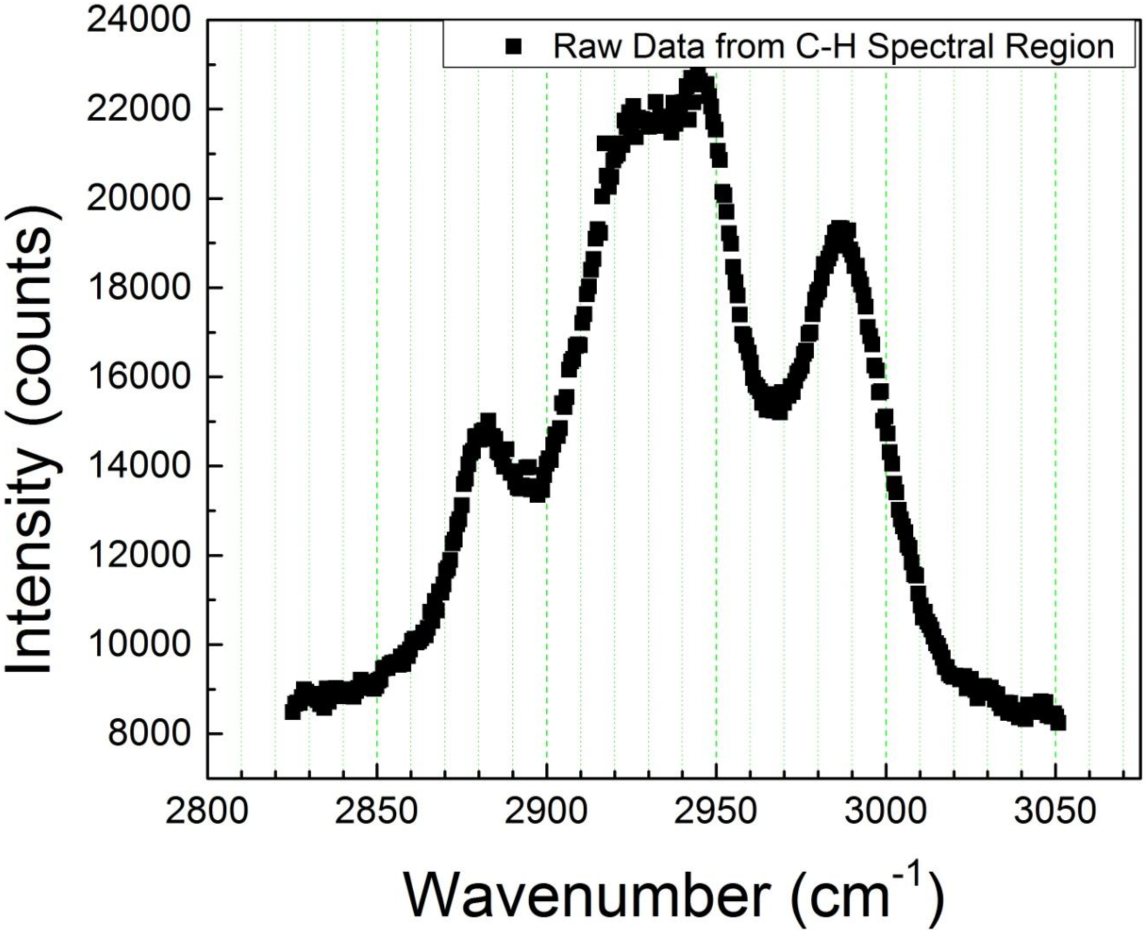

Figure 18: Raw data showing the C-H spectral region, taken from high resolution spectra of PNIPAM

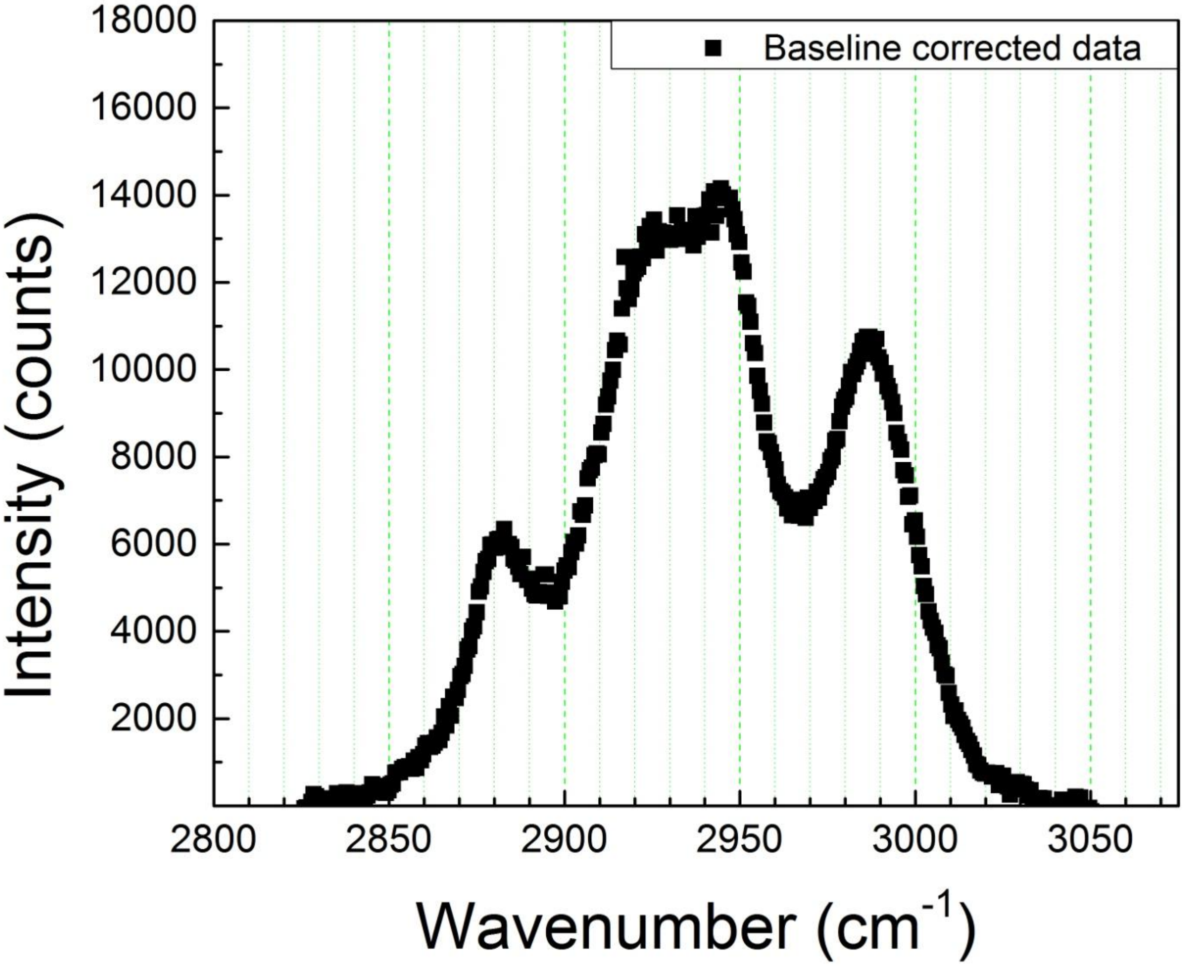

Figure 19: C-H data after performing baseline correction.

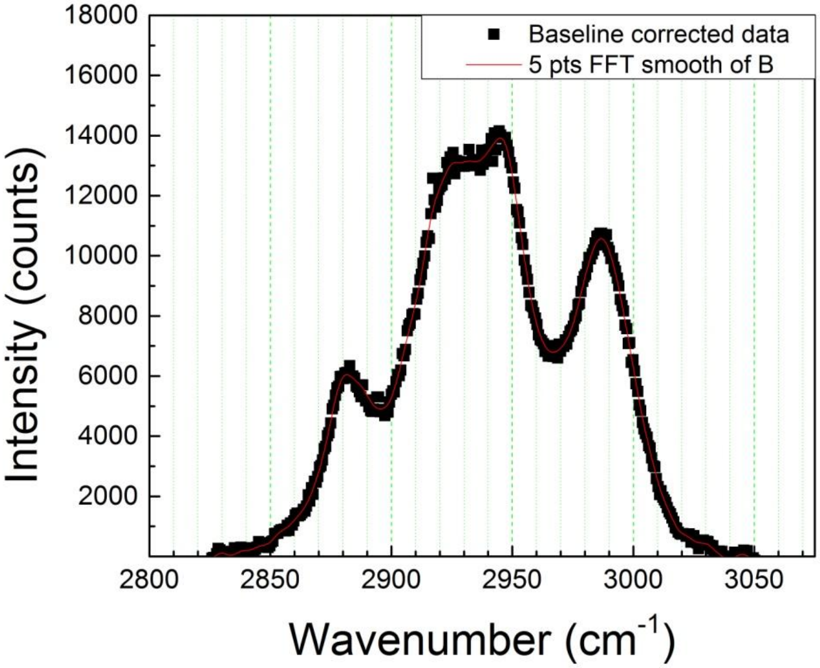

Figure 20: FFT smooth shown in red, superimposed onto baseline corrected data.

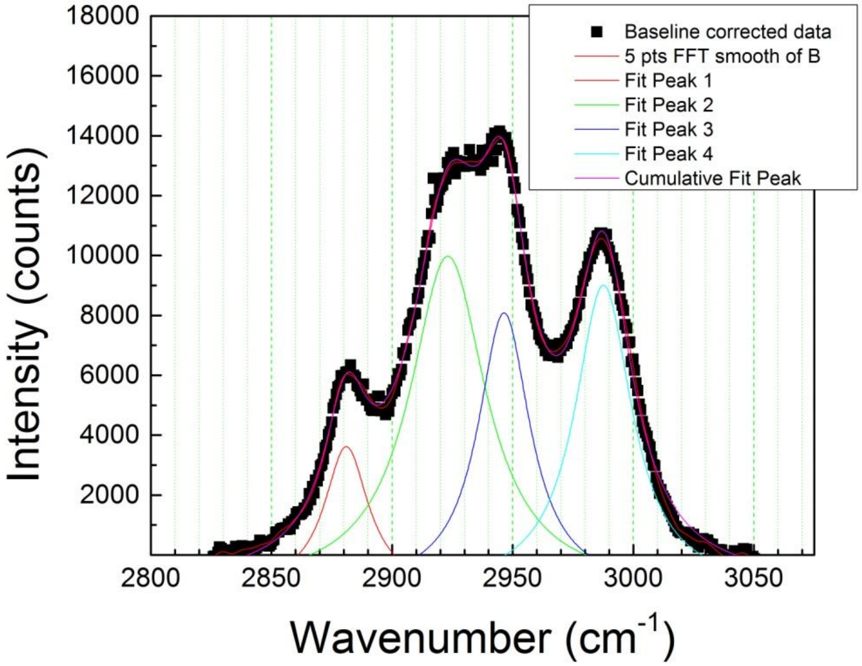

Figure 21: Fit of smoothed data using Lorentzian function.

Deconvolution of the data was done by using the analysis software to obtain a least squares fit to a minimum sum of peaks, in this case fitting the data to four Lorentzian functions (Figure 19). The Lorentzian function was chosen due to the similarity to the observed signal, as well as producing more consistent results and a visibly better fit than when using the Gaussian function. This was also the line shape chosen in previously published studies. (18) The natural line shape of Raman peaks is the Lorentzian, however it should be noted that often in practice signal broadening occurs due to heterogeneities in the sample. In these cases Voigtian functions may be more appropriate to use, and in certain limits can also be approximately Gaussian.

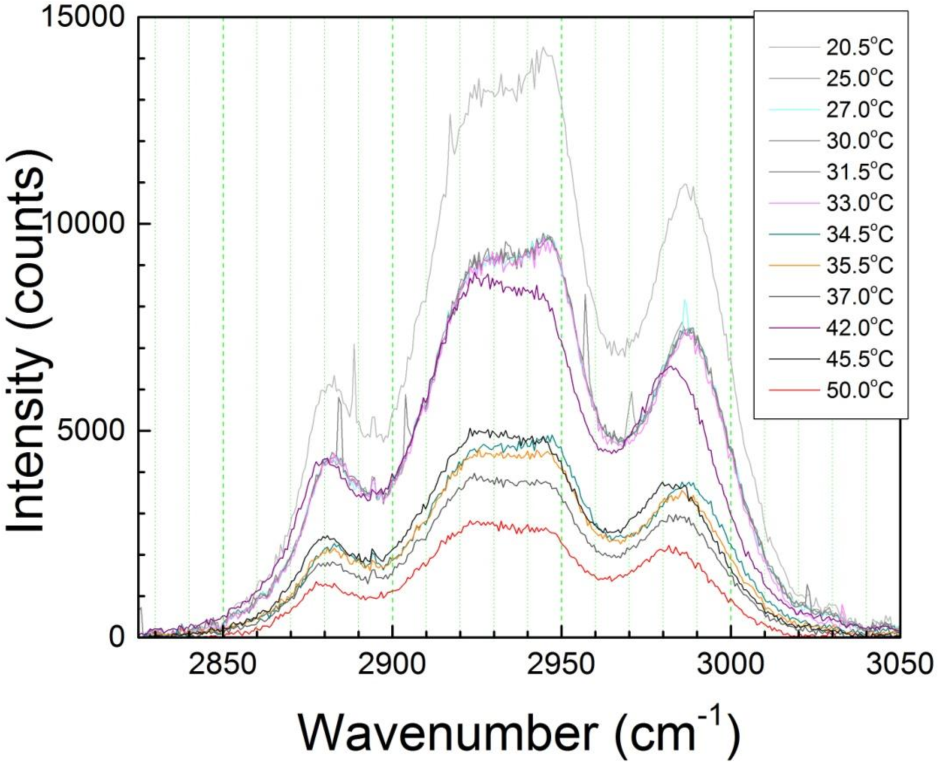

Figure 22: Plot of the C-H spectra region of PNIPAM at various temperatures.

Figure 22 shows the high resolution spectra of the C-H region acquired at various temperatures. From Table 1, we identify the peaks around 2880 and 2980cm^{-1} as being associated with the symmetric and asymmetric stretch modes of the hydrophobic methyl group. The peaks around 2920 and 2940cm^{-1} are assigned to the symmetric and asymmetric stretching vibrations of the C-H backbone of the PNIPAM molecule. Examination of the peak frequencies of the methyl groups' C-H stretching modes reveals a sharp downshift in frequency for both the asymmetric and symmetric modes, which can be observed in Figures 23 and 24.This downshift occurs abruptly at $32.5^{o}C$, where a discontinuous decrease in the optical transmission of the sample is also observed. In contrast, the backbone C-H vibrations do not show a dramatic frequency shift, rather a change in the relative areas of the 2920 and 2940cm^{-1} is observed across the LCST. The change in areas observed for these peaks is not discontinuous across the LCST, like the frequency shift noted in the methyl groups' C-H vibrations. Instead, the change in area appears to occur linearly with the increase in temperature, as can be seen in Figures 25 and 26. A molecular description explaining the discontinuous downshift the methyl groups' C-H stretch modes has not been decided on, however it is known to characterize the temperature induced phase transition. (16) (31) As we will see, results from the pressure phase transition along with these observations support the hypothesis that the frequency shifts seen in the methyl groups can be associated with the amount of water bound to the adjacent polar group.

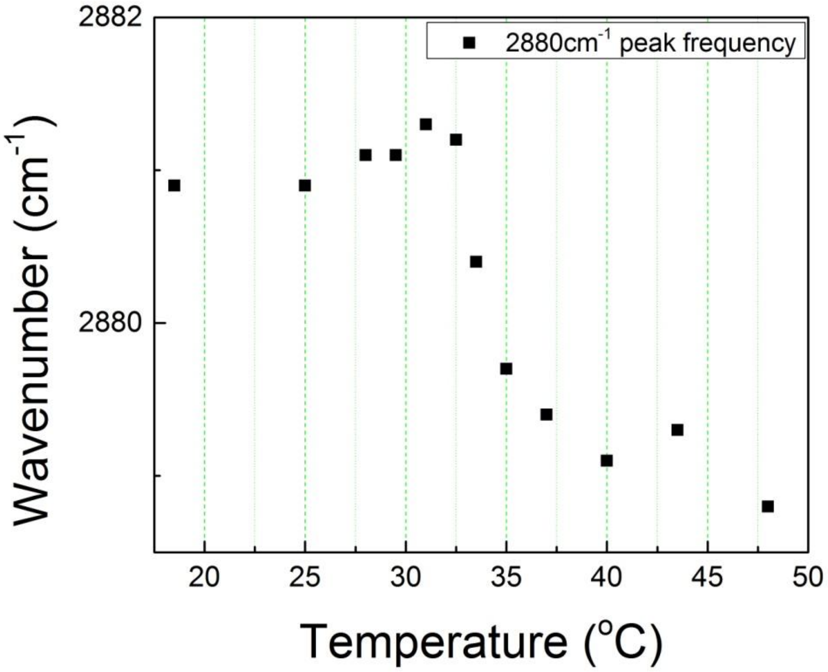

Figure 23: Peak frequency of the symmetric stretch mode of the hydrophobic methyl C-H bonds at various temperatures.

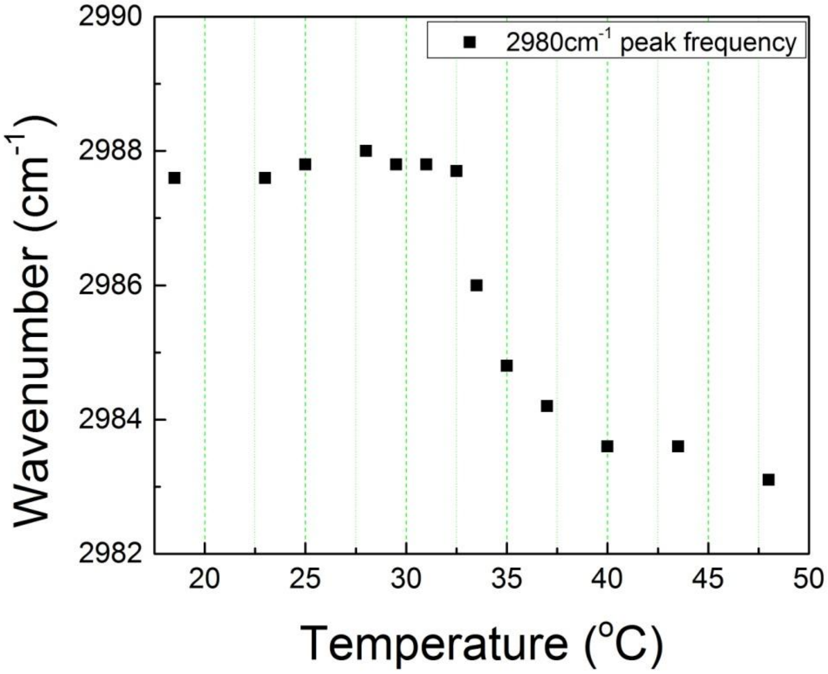

Figure 24: Peak frequency of the asymmetric stretching vibration of the hydrophobic methyl group at various temperatures.

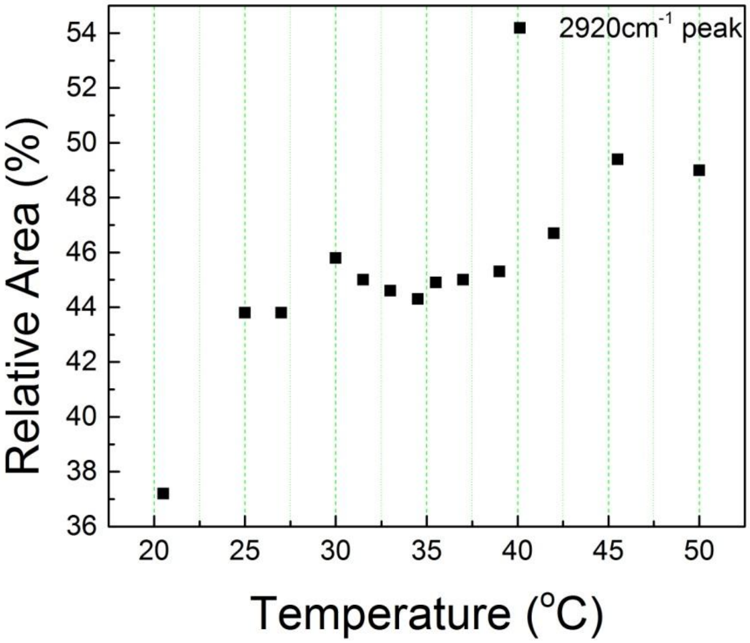

Figure 25: Relative area of the 2920cm^{-1} peak, belonging to the symmetric C-H stretching vibration of the isopropyl backbone, at various temperatures.

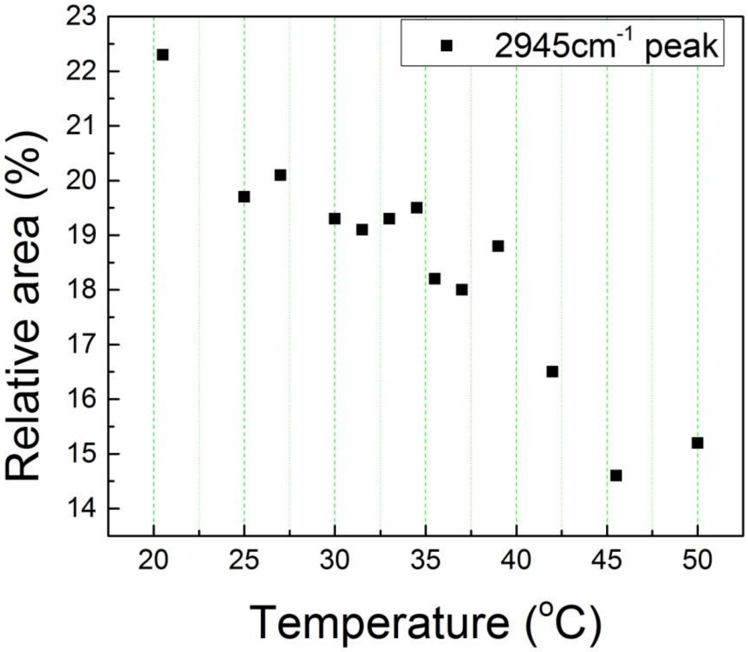

Figure 26: Relative area of the peak belonging to the asymmetric C-H stretching mode of the isopropyl backbone, at various temperatures.

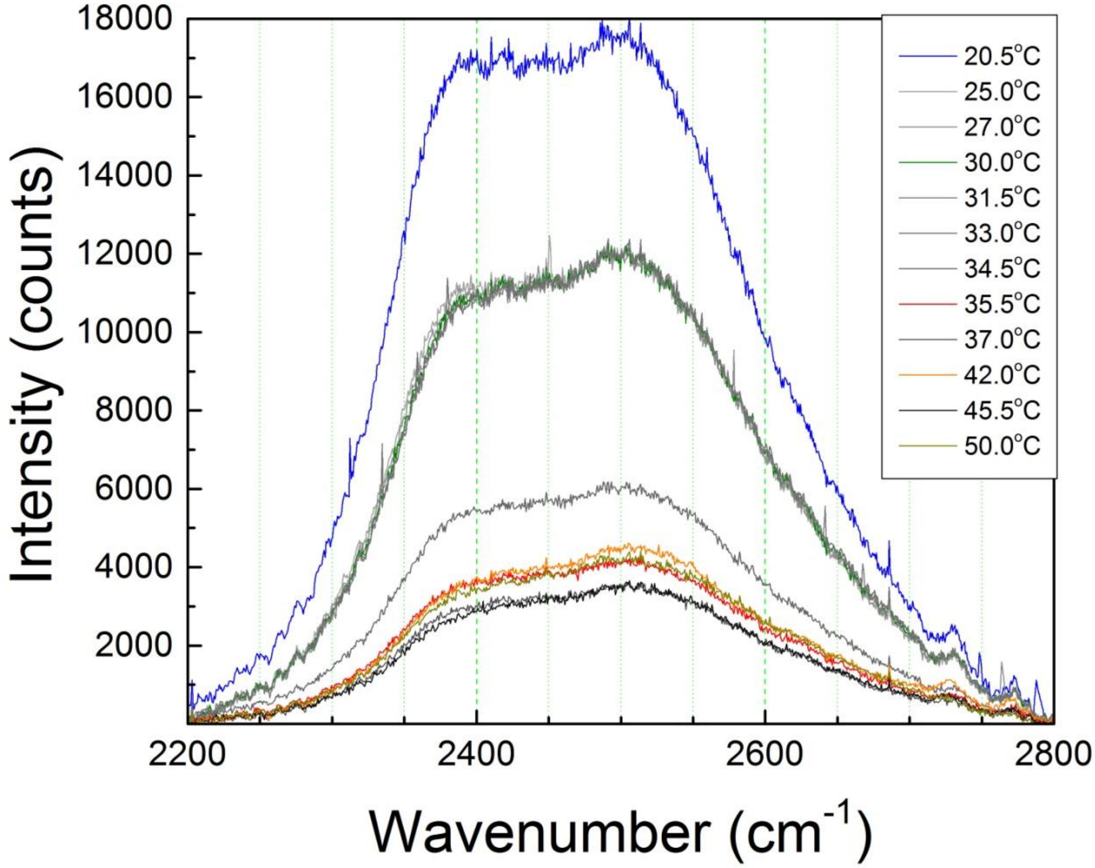

Figure 27: Raman spectra of the D_2O region of PNIPAM spectra, at various temperatures.

The D_2O spectral region of PNIPAM can be seen at various temperatures in Figure 27 above. We deconvolute the D_2O spectrum into 2 constituent Gaussian peaks, at 2380 and 2495cm^{-1}. The 2495cm^{-1} peak dominates the D_2O spectrum of PNIPAM, therefore likely originates in the bulk water. The 2380cm^{-1} peak contributes roughly 10% of the intensity to the D_2O spectral region, and can be seen to decrease in area as the temperature is lowered. This suggests a decrease in concentration of the corresponding species of D_2O molecules. Both of these vibrations increase monotonically in energy, as indicated by the upwards shift in frequency in Figures 28 and 29. The shift does not appear discontinuous across the phase transition. Figures

30 and 31 show the decrease in area of the 2380cm^{-1} peak along with the corresponding increase in the 2495cm^{-1} peak, indicative of a change in the relative concentrations of different species of D_2O. Okada et al. (32) interpreted Raman shifts in O-H stretch modes to characterize changes in hydrogen bond strength between water molecules, which is consistent with the loss of bound water molecules in PNIPAM at higher temperatures.

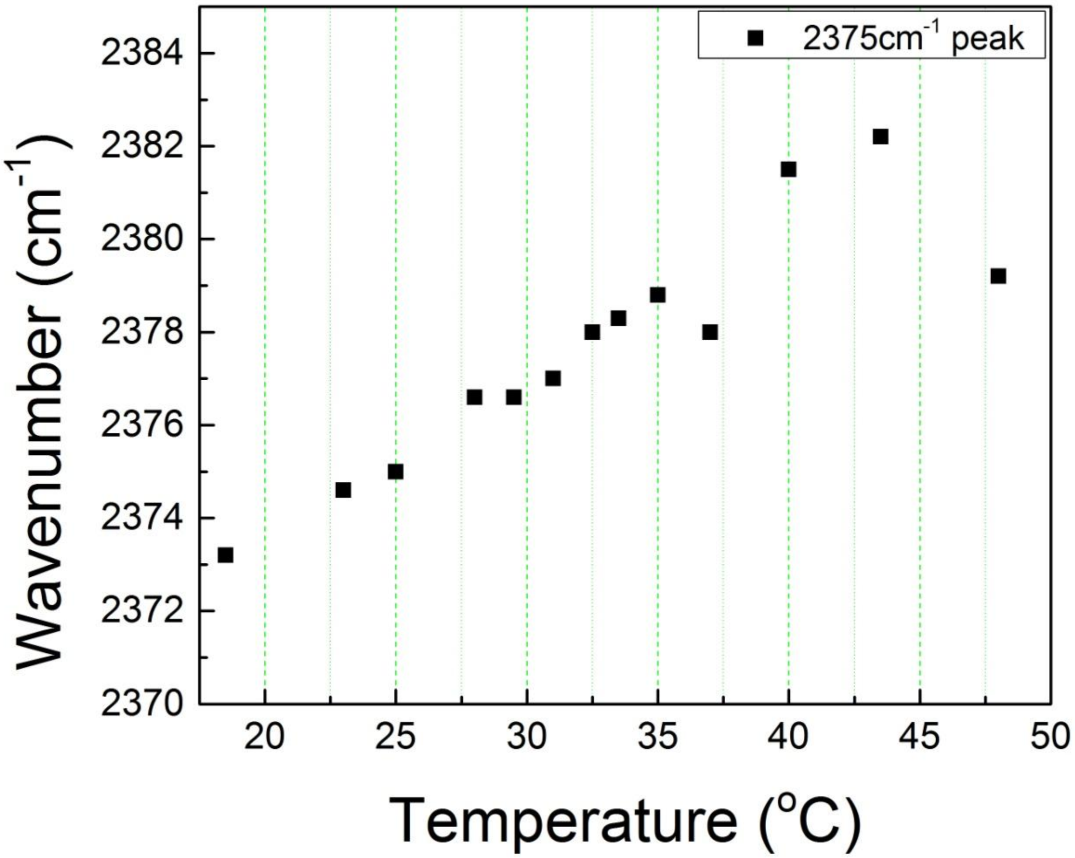

Figure 28: Frequency of the 2375cm^{-1} D_2O peak at various temperatures.

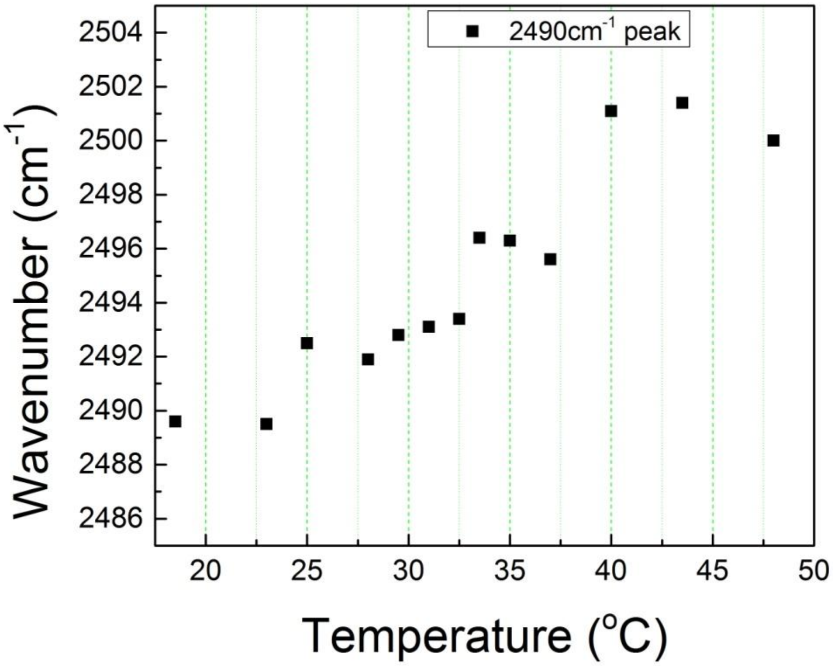

Figure 29: Frequency of the 2490$cm^{-1} D_2O$ peak at various temperatures.

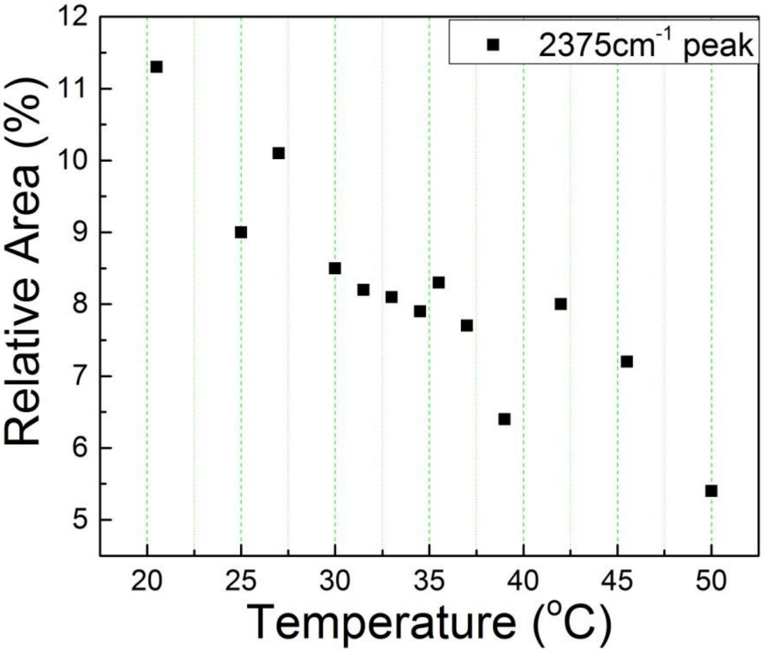

Figure 30: Relative area of the 2375cm^{-1} D_2O peak at various temperatures.

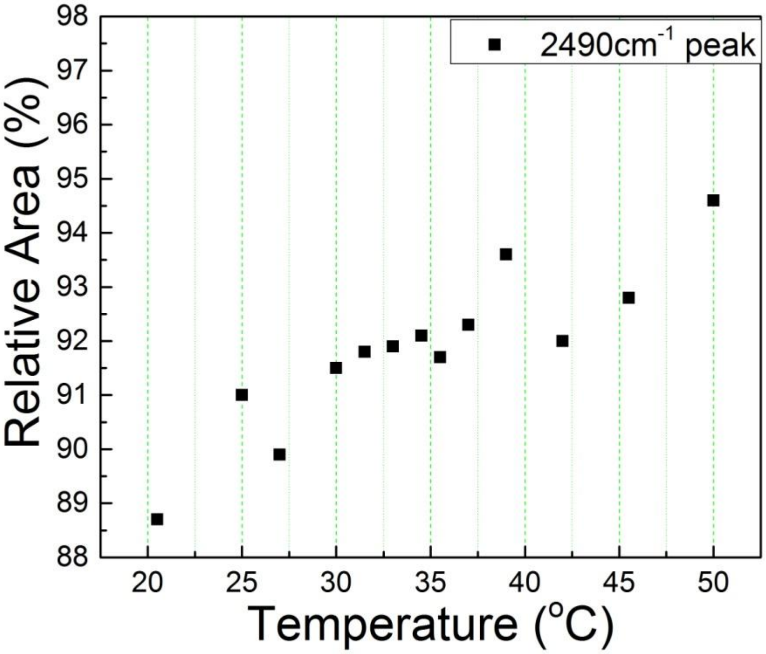

Figure 31: Relative area of the 2495cm^{-1} D_2O peak at various temperatures.

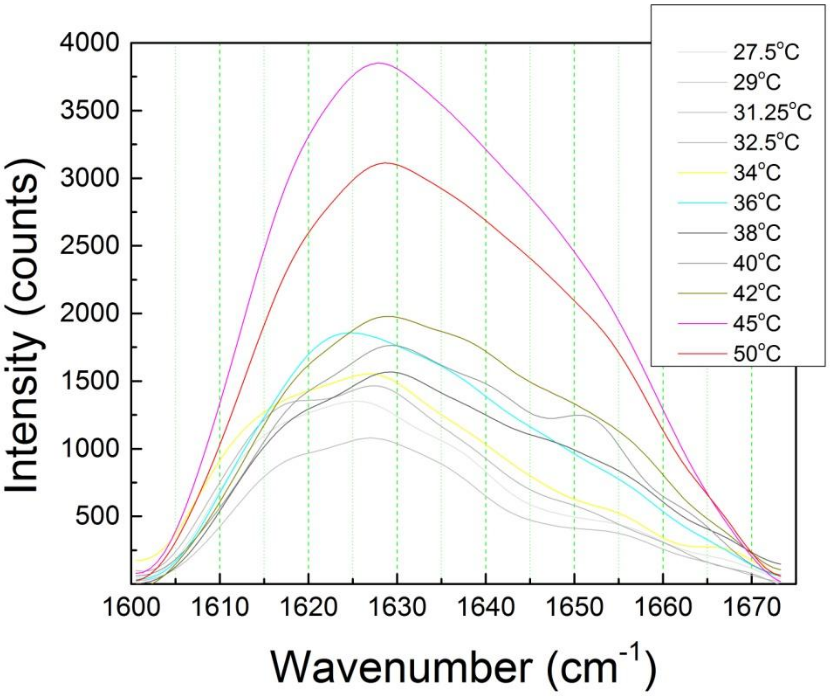

Figure 32: FFT smoothed Amide I' spectra at various temperatures.

In Figure 32, the amide I’ spectral differences across the LCST are noted. The peak situated at roughly 1625cm^{-1}, attributed to the carbonyl group hydrogen bonded with water (31), is more diffuse at lower temperatures. This is likely from interactions of the group with other nucleated water molecules. At higher temperatures the peak becomes more well-defined, and another peak at around 1650cm^{-1} increases in area relative to the peak at 1625cm^{-1}. Manas et al. observed a upshift of $25cm^{-1}$ in the frequency of the amide I band when a protein buries the polar group inside its hydrophobic core. (33) The sharpening of the 1625cm^{-1} peak can be explained by a loss of additional bound water molecules, and the 1650cm^{-1} is thought to characterize a coil to globule transition in the PNIPAM. (16) (17) Similarly, Asher et al. proposed the formation of hydrophobic nano-pockets in PNIPAM above the LCST, with the polar groups buried inside. (18)

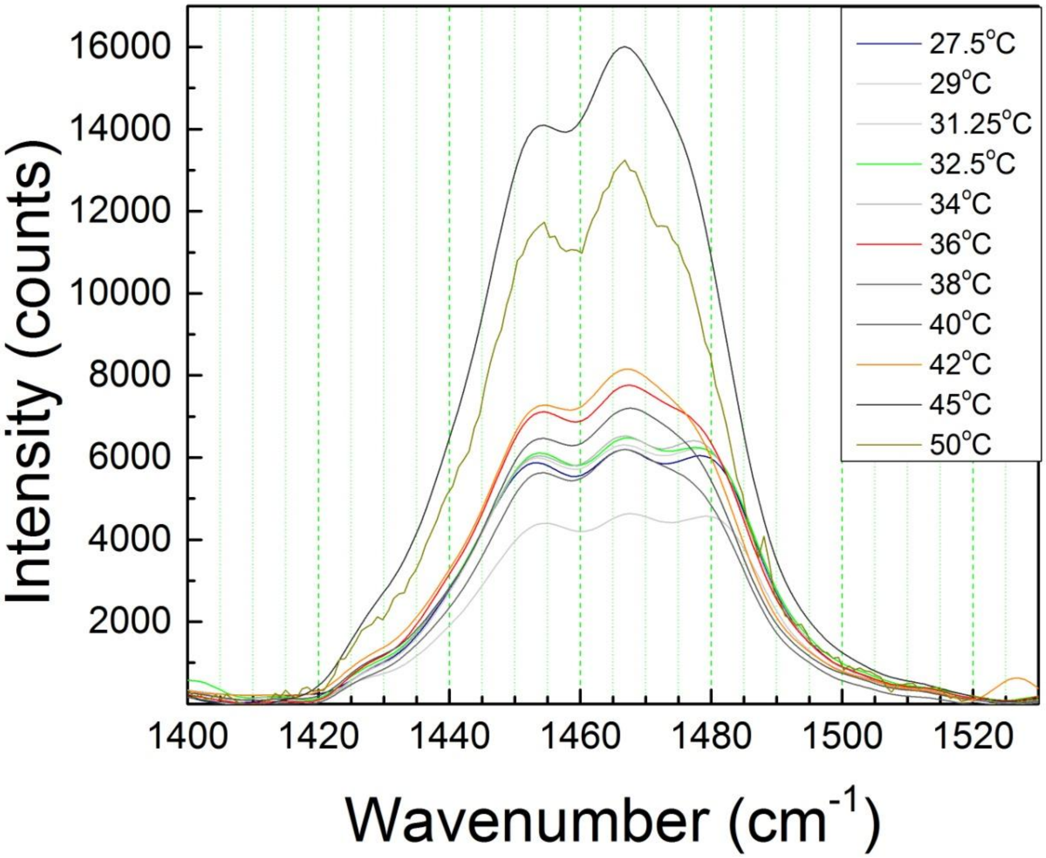

Figure 33: FFT smoothed spectra of C-H spectral region at various temperatures.

Figure 33 shows the spectral region containing contributions from the C-H deformation modes of the hydrophobic group at $1480 cm^{-1}$, the backbone at $1460 cm^{-1}$, and an unassigned contribution at $1450 cm^{-1}$. The latter Raman peak is an example of a Raman active mode that is not seen in absorption measurements due to the difference in selection rules (Figure 12). The spectral shifts are similar to those observed in the C-H modes found at higher wavenumbers, with the backbone peak showing a large increase in area and the frequency assigned to the methyl group showing a discontinuous downshift across the LCST.

3.2.2 Analysis of the Pressure Induced VPT

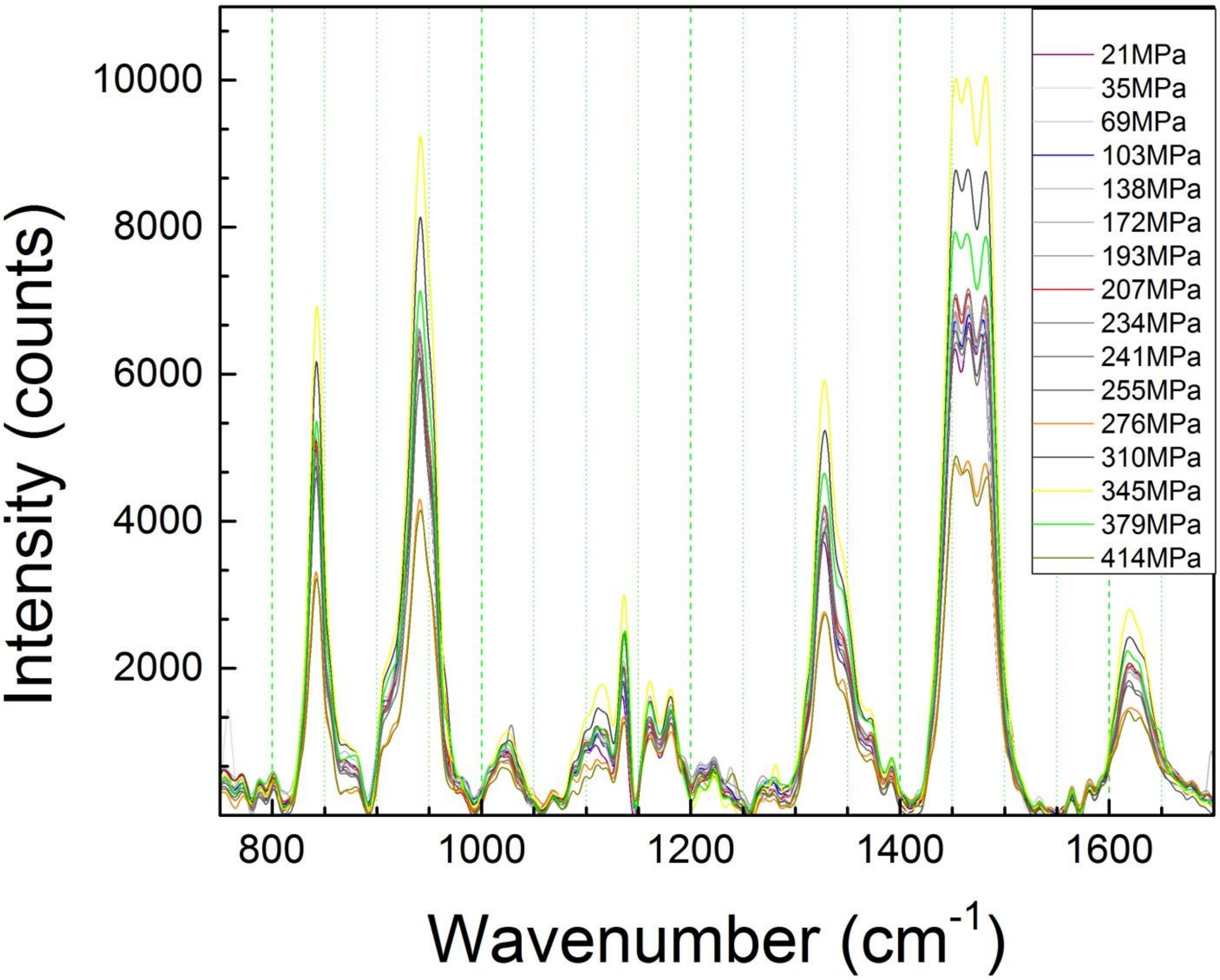

Figure 34: Raman spectra of PNIPAM in the fingerprint spectral region at various pressures

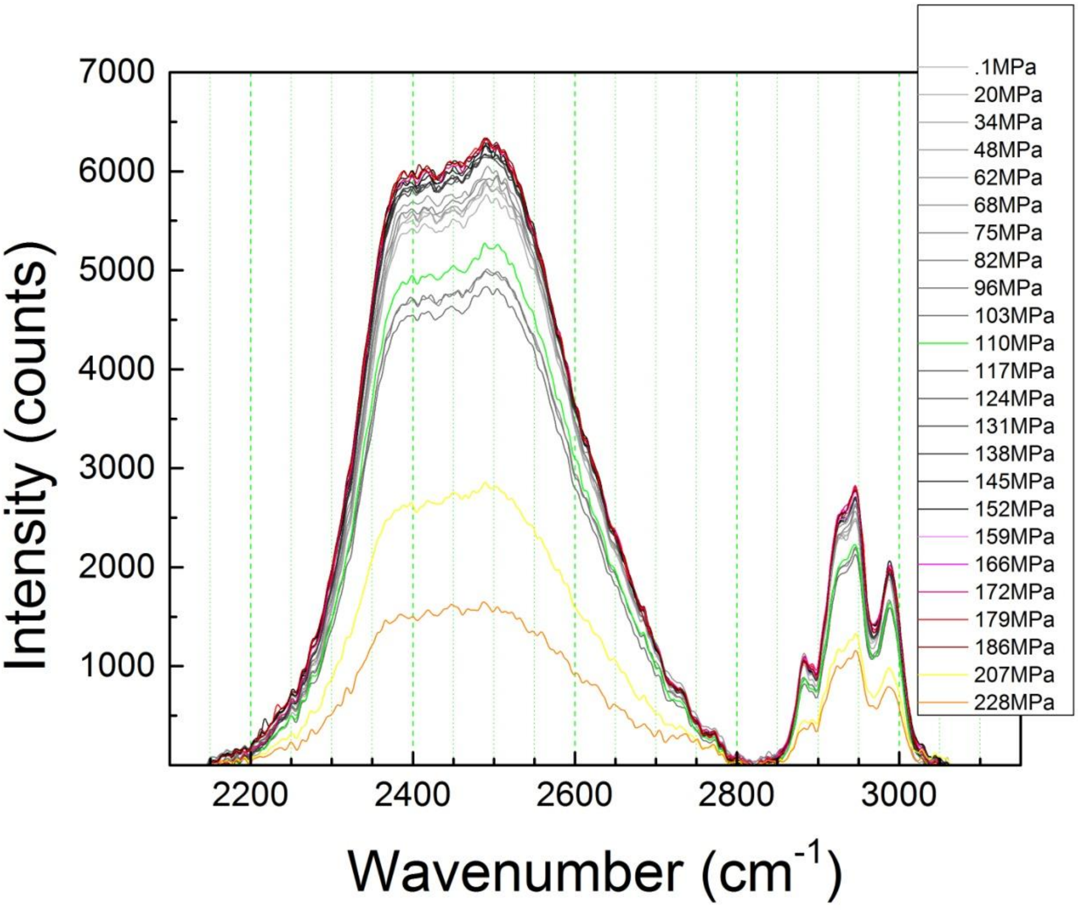

Figure 35: Raman spectra of PNIPAM in the D_2O/C-H spectral region at various pressures.

We now examine the spectra of PNIPAM across the pressure induced phase transition, shown in Figures 34 and 35. We analyze the spectral shifts observed in the C-H and D_2O regions and look qualitatively at the amide I and C-H deformation modes in the fingerprint region. The changes noted in the amide I, C-H, and D_2O spectral regions across the temperature induced VPT are absent in the high pressure spectra after phase separation. The frequencies of the water peaks shift down monotonically with increasing pressure until about 200MPa, in contrast with the case of increasing temperatures, where an upshift in frequency was observed. The relative areas of the water peaks remained stable across the observed pressure transition, where we saw a marked decrease in the relative area of the $2375cm^{-1}$ peak above the LCST.

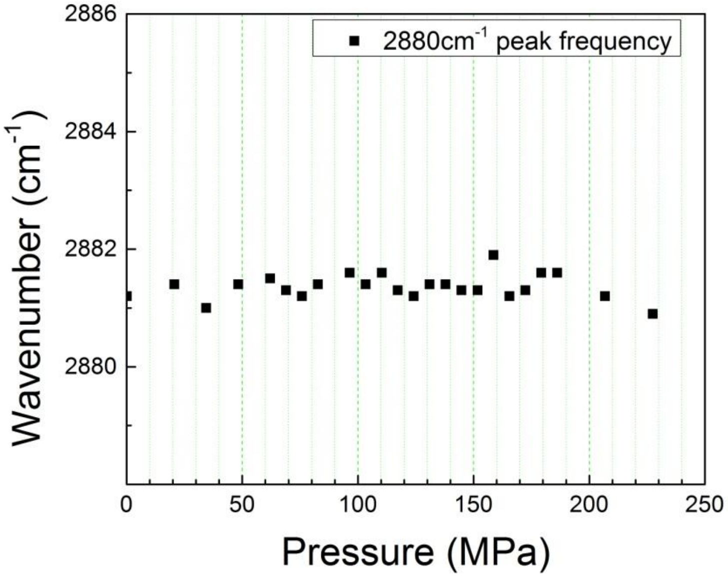

Figure 36: Frequency of the $2880cm^{-1}$ peak at various pressures.

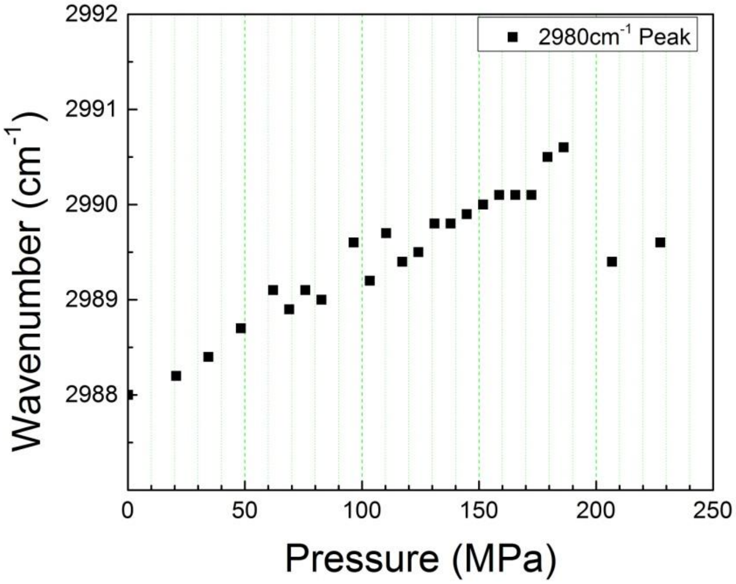

Figure 37: Frequency of the $2980cm^{-1}$ peak at various pressures.

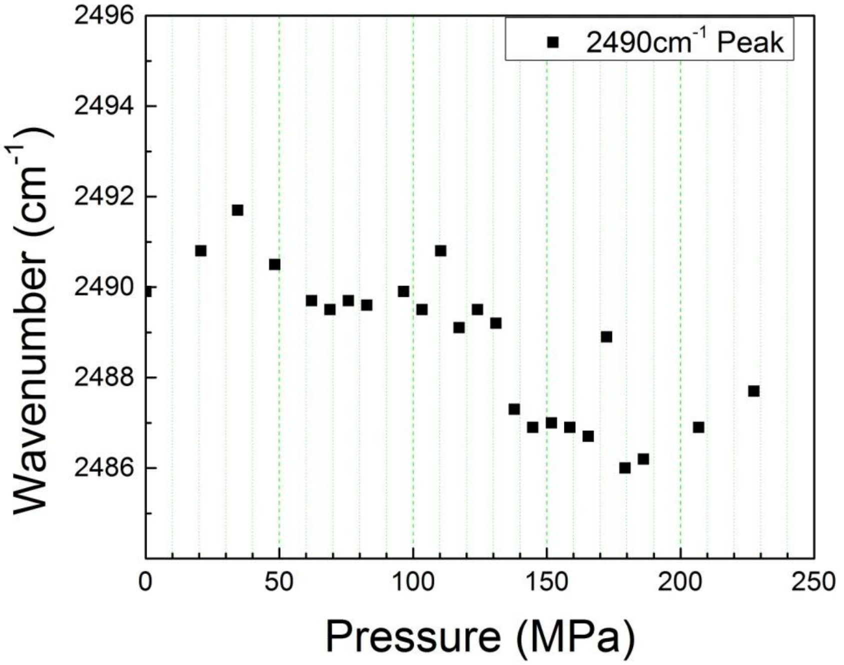

Figure 38: Frequency of the 2490cm^{-1} peak at various pressures.

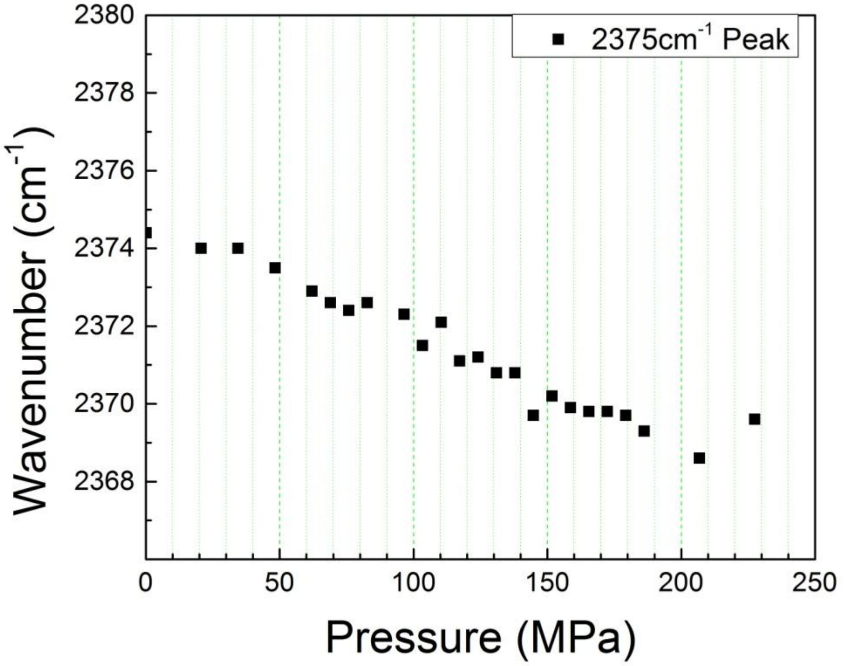

Figure 39: Frequency of the 2375cm^{-1} peak at various pressures.

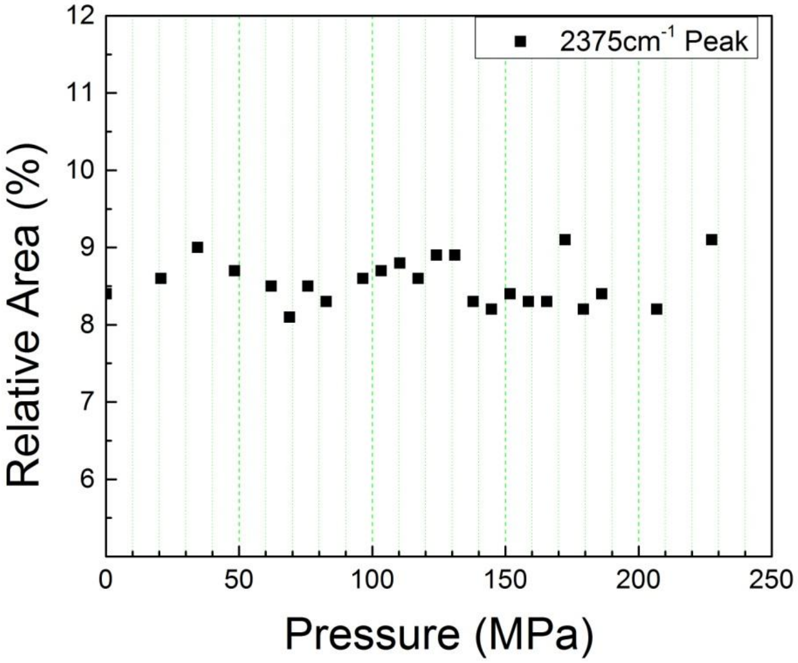

Figure 40: Relative area of the 2375cm^{-1} D_2O Raman peak at various pressures.

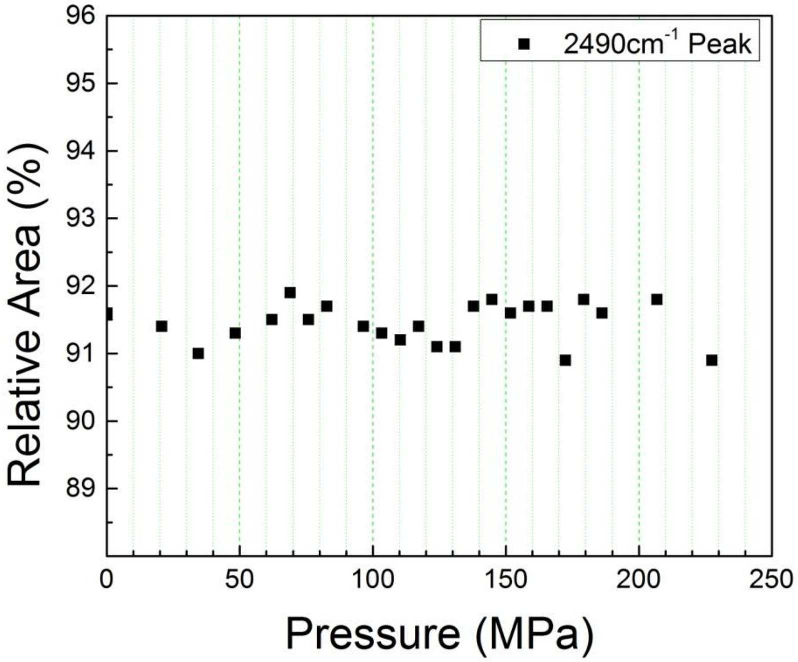

Figure 41: Relative area of the 2490cm^{-1} D_2O Raman peak at various pressures.

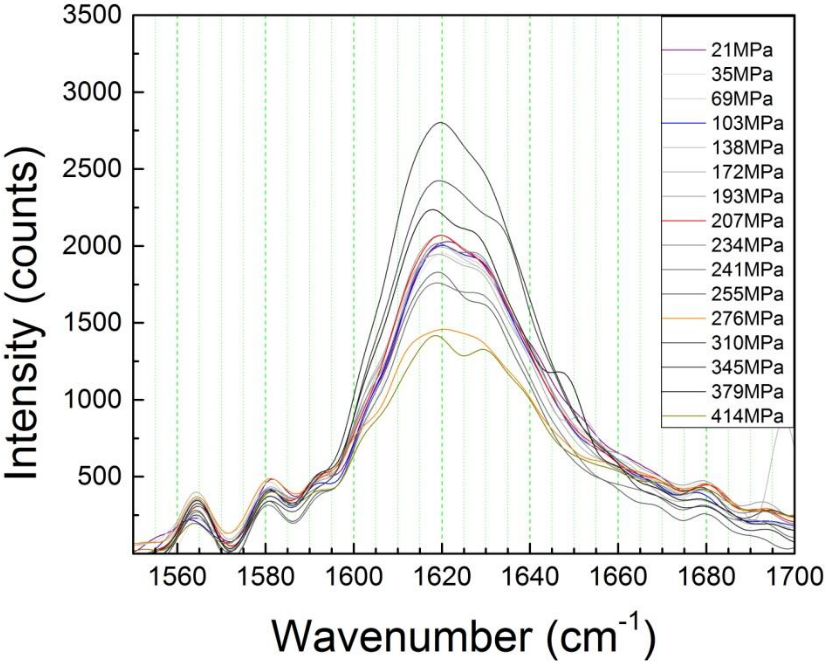

Figure 42: Amide I' spectral region at various pressures.

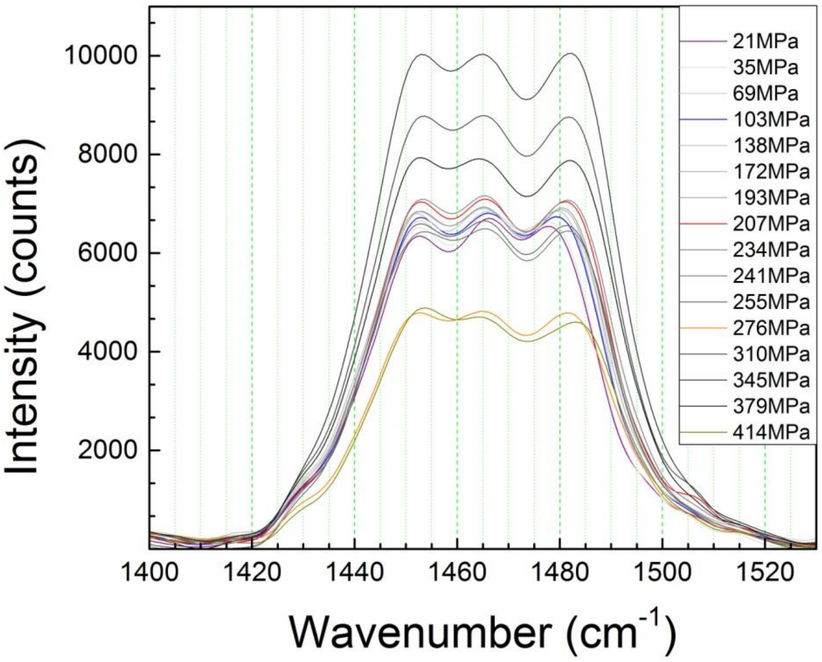

Figure 43: Spectral region containing contributions from methyl and backbone C-H groups at various pressures.

In the C-H spectral region, the peak at $2880cm^{-1}$remains stable at the pressure was increased. The $2980cm^{-1}$ peak frequency, on the other hand, increases linearly with the increase in pressure. These results agree with FTIR data acquired by Heremans et al., where a diamond anvil cell was used to pressurize the sample. (6) The C-H spectral region at lower wavenumbers, shown in Figure 38, shows the same behavior. The frequency of the O-D stretch modes decreases monotonically until around 200MPa, where an upshift in frequency with pressure is seen. Okada et al. found similar results in Raman experiments using a commercial stainless steel pressure cell capable of withstanding higher pressures than our fused silica capillaries yet not so well-suited for microscopic measurements, having a 7mm thick sapphire window. They interpreted the downshift in frequency at moderate pressures (<150MPa) to characterize the increasing strength of hydrogen bonding between D_2O molecules, then increasing between 150 and 300MPa, then decreasing again at higher pressures. (32) They offer the interpretation of the O-H stretch spectral region as having contributions from hydrogen bonded (polymer) and non-hydrogen bonded (monomer) water molecules, with the former having a lower peak frequency, and also propose a pressure dependence on the average coordination of the water molecules. This supports the hypothesis that the frequency of the methyl groups in PNIPAM depends in part on the number of water molecules bound to the adjacent polar groups. A strengthening of hydrogen bonding at moderate pressures would result in more bound water molecules at the polar groups, which matches the observed upshift in frequency. Furthermore, the drop in the C-H stretch mode at a 200MPa coincides with the pressure at which the O-D stretch frequencies begin to upshift.

The change in the relative intensities of the $2920cm^{-1}$ and $2940cm^{-1}$ peaks seen across the LCST transition was not observed as the pressure was increased. Since these frequencies are attributed to the isopropyl groups, it demonstrates the same distribution of Ramachandran angles before and after the pressure-induced phase transition. In other words, the random coil configuration is maintained across the phase transition. The amide I spectral region, shown in Figure 40, also provides evidence for this. The increase in the area of the $1650cm^{-1}$ peak that we observed across the temperature transition is not observed with an increase in pressure. This is evidence that formation of hydrophobic nano-pockets, believed to occur across the LCST transition, does not occur during the pressure induced phase transition.

3.3 Conclusion

In this thesis we report results on the temperature and pressure dependence of the Raman spectra of PNIPAM, as well as microscopic imaging showing the evolution of phase transition induced by temperature and pressure. The temperature results are in good agreement with previously published studies and validate the analysis techniques used for both the temperature and pressure experiments. Results from the pressure experiments corroborate similar experiments performed with FTIR, QENS, and cloud point measurements (16) (3) (6), supplementing the FTIR data and requiring less baseline correction in certain spectral regions. Additional vibrational bands are investigated that are excluded from FTIR analysis due to the difference in absorption and Raman selection rules.

Our Raman measurements of the D_2O region point to a strengthening of the hydrogen bonds in water with increased pressure, concurring with other pressure experiments done on water.

Conversely, the loss of bound water noted across the LCST is apparently the primary driving mechanism for the temperature transition. Thus the evolution of the pressure induced phase transition is markedly different from the evolution of the system with increasing temperature, with microscopic imaging suggesting that the pressure transition evolves via spinodal decomposition. Also, the discontinuous downshift in the C-H vibration of the hydrophobic group does not occur across the pressure induce phase transition, suggesting that the hydrophobic pockets formed during the collapse of the PNIPAM molecule at high temperatures, which stabilize the collapsed state, are not similarly formed at high pressures. Also, the discontinuous shift in the two constituent Amide I' peak areas, noted across the LCST, is absent. It has been suggested that PNIPAM remains in a coil-like configuration at higher pressures (6) (34); the lack of change in the C-H backbone spectra (noted across the LCST) and the absence of a peak at $1650cm^{-1}$ across the pressure transition further assert the veracity of this claim.

References

1. *Poly(N-Isopropylacrylamide): Experiment, Theory, and Application.* **Schild, H. G.** Cambridge, MA : Prog. Polym. Sci., 1992, Vol. 17. 163-249.

2. *A new insight into the understanding of the collapsed form of Poly(N-isoproylacrylamide) molecules.* **A. Esteve, A. Bail, A. Dkhissi, M. Djafari Rouhani, J. Sudor, A.M. Gue.** November 2007, Journal of Chemical Physics, 340 (1), pp. 12-16.

3. *Influency of high-pressure on cononsolvency of poly(N-isopropylacrylamide) nanogels in water/methanol mixtures.* **C. Hofmann, S. Grobelny, M. Erlkamp, and R. Winter.** 55, s.l. : Polymer, 2014. 2000-2007.

4. *A Novel Application of Two-Dimensional Correlation Infrared Spectroscopy: Exploration of the Reversibility of the Pressure- and Temperature-Induced Phase Separation of Poly(N-Isopropylacrylamide) and Poly(N-Isopropylmethacrylamide) in Aqueous Solution.* **Y. Wu, P. Meersman, and Y. Ozaki.** s.l. : Macromolecules, 2006, Vol. 39. 1182-1188.

5. *Quasi-Elastic Neutron Scattering Study on Water and Polymer Dynamics in Thermo/Pressure Sensitive Polymer Solutions.* **N. Osaka, M. Shibayama, T. Kikuchi, and O. Yamamuro.** B, s.l. : J. Phys. Chem., 2009, Vol. 113. 12870-12876.

6. *Pressure Effects on the Hydration Properties of Poly(N-isopropylacrylamide) in Aqueous Solution Studied by FTIR Spectroscopy.* **F. Meersman, J. Wang, Y. Wu, and K. Heremans.** 2005, Macromolecules, 38, pp. 8923-8928.

7. **H. Frauenfelder, S. S. Chan, and W. S. Chan.** *The Physics of Proteins.* Springer, NY : Springer, 2010. ISBN 978-1-4419-1044-8.

8. *The pressure dependence of hydrophobic interactions is consistent with the observed pressure denaturation of proteins.* **G. Hummer, S. Garde, A. E. Garcia, M. E. Paulaitis, and L. R. Pratt.** Biophysics, s.l. : Proc. Natl. Acad. Sci. USA, February 1998, Vol. 95. 1552-1555.

9. *High pressure effects on biological macromolecules: from structulal changes to alteration of cellular processes.* **C. Balny, P. Masson, and K. Heremans.** 1595, s.l. : Biochimica et Biophysica Acta, 2002. 3-10.

10. **Jones, Richard A. L.** *Soft Condensed Matter.* Oxford : Oxford, 2002.

11. **Flory, P.J.** *Principles of Polymer Chemistry.* Ithaca, NY : Cornell University Press, 1953.

12. **Rupp, Bernhard.** Physical Chemistry of Protein Crystallization. [Online] University of California, 2000. [Cited: 6 12, 2014.] http://www.ruppweb.org/Xray/tutorial/PC_of_crystallization.htm#_Toc485292934.

13. **Novick-Cohen, A.** *Handbook of Differential Equations.* s.l. : Elsevier, 2008. 1874-5717(08)00004-2.

14. *Spontaneous rapid phase separation induced by rapid hydrodynamic coarsening in two-dimensional fluid mixtures.* **Tanaka, H and Araki, T.** 2, s.l. : Physical Review Letters, 1998, Vol. 81. 389-392.

15. *Hydration, phase separation and nonlinear rheology of temperature-sensitive water-soluble polymers.* **F. Tanaka, T. Koga, I. Kaneda, and F. Winnik.** s.l. : J. Phys.: Condens. Matter, 2011, Vol. 23. 284105.

16. *A FTIR and 2D-IR Spectroscopic Study on the Microdynamics Phase Separation Mechanism of the Poly(N-isopropylacrylamide) Aqueous Solution.* **B. Sun, Y. Lin, P. Wu, and H. W. Siesler.** s.l. : Macromolecules, 2008, Vol. 41. 1512-1520.

17. *Role of Bound Water and Hydrophobic Interaction in Phase Transition of Poly(N-isopropylacrylamide) Aqueous Solution.* **E. C. Cho, J. Lee, and K. Cho.** 36, s.l. : Macromolecules, 2003. 9929-9934.

18. *UV Resonance Determination of Molecular Mechanism of Poly(N-Isopropylacrylamide) Volume Phase Transition.* **Z. Ahmed, E. A. Gooding, K. V. Pimenov, L. Wang, and S. A. Asher.** B, s.l. : J Phys. Chem., 2009, Vol. 113 (13). 4248-4256.

19. *Volumetric Studies of Aqueous Polymer Solutions Using Pressure Perturbation Calorimetry: A New Look at the Temperature-Induced Phase Transition of Poly(N-isopropylacrylamide) in Water and D2O.* **Winnik, P. Kujawa and F. M.** 34, s.l. : Macromolecules, 2001. 4130-4135.

20. *Contrary hydration behavior of N-isopropylacrylamide to its polymer, P(NIPAm), with a lower critical solution temperature .* **Shitaka, Y. Ono and T.** s.l. : J. Chem. Phys. B., 2007, Vol. 111 (7). 1511-1513.

21. *Differences in pressure and temperature transitions of proteins and polymer gels.* **S. Kunugi, K. Kameyama, T. Tada, N. Tanaka, M. Shibayama, and M. Akashi.** 38, s.l. : Brazilian Journal of Medical and Biological Research , 2005. 1233-1238.

22. *A New Type of Secondary Radiation.* **Raman, C.V. and Krishnan, K.S.** 501-502, s.l. : Nature, 1928, Vol. 121.

23. **Lewis, Ian R. and Edwards, Howell G. M.** *Handbook of Raman Spectroscopy.* New York : Marcel Dekker, Inc., 2001.

24. UCSB Gordon Research Goup. [Online] University of California, Santa Barbara, 2012. [Cited: August 25, 2014.] http://www.engr.ucsb.edu/~mjgordon/research/raman.html.

25. *Vibrational Spectroscopy of Polymers.* **Siesler, H. W.** s.l. : International Journal of Polymer Anal. Charact., 2011, Vol. 16. 519-541.

26. **McCreery, Richard.** *Raman Spectroscopy for Chemical Analysis.* New York : John Wiley & Sons, 2000.

27. *Micro-raman spectroscopy in the undergraduate research laboratory.* **Voor, R., Chow, L. and Schulte, A.** Orlando : American Jounal of Physics, 1993, Vol. 62. 5.

28. *Proc. XXIIth Intl. Conf. on Raman Spectroscopy.* **S.H. Park, T. Oakeson, A. Schulte.** 2010. vol 1267, 662-663.

29. *Pressure Effects on the Aggregation of Poly(N-isoproylacrylamide) and Poly(N-isopropylacrylamide-co-acrylic acid) in Aqueous Solutions.* **K. Otake, R. Karaki, T. Ebina, C. Yokoyama, and S. Takahashi.** 26, s.l. : Macromolecules, 1993. 2194-2197.

30. *Structure Analysis of Poly(N-isopropylacrylamide) Using Near Infrared Spectroscopy and Generalized Two-Dimensional Correlation Spectroscopy.* **B. Sun, Y. Lin and P. We.** 2007, Applied Spectroscopy, Volume 61, Number 7.

31. **Schulte, A. et al.** FTIR. *DPG Spring Meeting.* 2014.

32. *Change in Hydration State during Coil-Globule Transition of Aqueous Solutions of Poly(N-isopropylacrylamide) as Evidenced by FTIR Spectroscopy.* **Y. Maeda, T. Higuchi, and I Ikeda.** s.l. : Langmuir, 2000, Vol. 16. 7503-7509.

33. *Pressure response of Raman spectra of water and its implication to the change in hydrogen bond interaction.* **T. Okada, K. Komatsu, T. Kawamoto, T. Yamanaka, and H. Kagi.** 61, s.l. : Elsevier, 2005, Vol. Spectrochimica Act A Part A. 2423-2427.

34. *Infrared Signature and Folding Dynamics of a Helical Beta-Peptide.* **E. S. Manas, Z. Getahun, W. W. Wright, W. F. DeGrado, and J. M. Vanderkooi.** s.l. : J Am Chem Soc., 2000, Vol. 122. 9883.

35. *Simulations of the pressure and temperature unfolding of an alph-helical peptide.* **D. Paschek, S. Gnanakaran, and A. E. Garcia.** 19, s.l. : PNAS, 2005, Vol. 102. 6765-6770.

36. *Nobel Lecture.* **Flory, P.J.** 1974.

37. *Phase Transition of N-Substituted Acrylamide Gels.* **H. Inomata, S. Goto, and S. Saito.** s.l. : Macromolecules, 1990, Vol. 23. 4887-4888.

38. *LCST and UCST Behavior of Poly(N-isopropylacrylamide) in DMSO/Water Mixed Solvents Studied by IR-and Micro-Raman Spectroscopy.* **Maeda, H. Yamauchi and Y.** B, s.l. : J. Phys. Chem, 2007, Vol. 111. 12964-12968.

39. *Phase Separation in Semidilute Aqueous Poly(N-isopropylacrylamide) Solutions.* **A. Meier-Koll, V. Pipich, P. Busch, C. M. Papadakis, and P. M. Buschbaum.** 28, s.l. : ACS/Langmuir, 2012. 8791-8798.